Check for updates

The Journal of Physiology

Differential effects of mechano-electric feedback mechanisms on whole-heart activation, repolarization, and tension

Tobias Gerach and Axel Loewe

Institute of Biomedical Engineering, Karlsruhe Institute of Technology (KIT), Karlsruhe, Germany

Handling Editors: Natalia Trayanova & Eilidh MacDonald

The peer review history is available in the Supporting Information section of this article (https://doi.org/10.1113/JP285022#support-information-section).

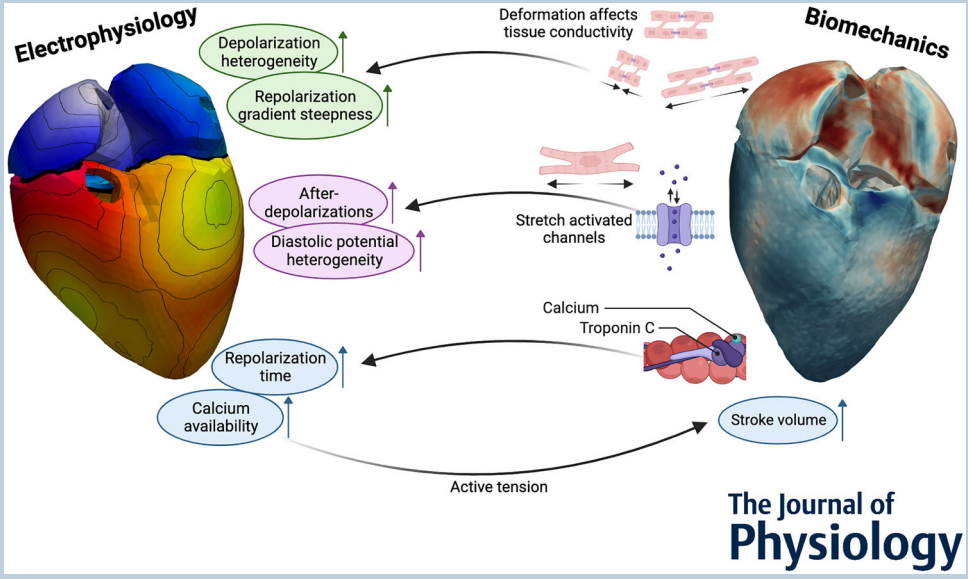

Abstract The human heart is subject to highly variable amounts of strain during day-to-day activities and needs to adapt to a wide range of physiological demands. This adaptation is driven by an autoregulatory loop that includes both electrical and the mechanical components. In particular, mechanical forces are known to feed back into the cardiac electrophysiology system, which can result in pro- and anti-arrhythmic effects. Despite the widespread use of computational modelling and simulation for cardiac electrophysiology research, the majority of *in silico* experiments

Tobias Gerach is a postdoctoral researcher at the Institute of Biomedical Engineering, Karlsruhe Institute of Technology (KIT). He earned his PhD in electrical engineering from KIT conducting research on personalized electromechanical modelling of the human heart, supervised by PD Dr Axel Loewe and Professor Dr Olaf Dössel. His research employed computational modelling to measure how changes in electromechanical properties of the heart, such as scar tissue, impact its overall function.

Software: The finite element software for electromechanical heart simulations is available at https://github.com/KIT-IBT/CardioMechanics. Fibre generation software is available at https://github.com/KIT-IBT/LDRB_Fibers for the ventricles and https://github.com/KIT-IBT/RESILIENT for the atria.

© 2024 The Authors. *The Journal of Physiology* published by John Wiley & Sons Ltd on behalf of The Physiological Society. DOI: 10.1113/JP285022

This is an open access article under the terms of the Creative Commons Attribution License, which permits use, distribution and reproduction in any medium, provided the original work is properly cited.

ignore this mechano-electric feedback entirely due to the high computational cost associated with solving cardiac mechanics. In this study, we therefore use an electromechanically coupled whole-heart model to investigate the differential and combined effects of electromechanical feedback mechanisms with a focus on their physiological relevance during sinus rhythm. In particular, we consider troponin-bound calcium, the effect of deformation on the tissue diffusion tensor, and stretch-activated channels. We found that activation of the myocardium was only significantly affected when including deformation into the diffusion term of the monodomain equation. Repolarization, on the other hand, was influenced by both troponin-bound calcium and stretch-activated channels and resulted in steeper repolarization gradients in the atria. The latter also caused afterdepolarizations in the atria. Due to its central role for tension development, calcium bound to troponin affected stroke volume and pressure. In conclusion, we found that mechano-electric feedback changes activation and repolarization patterns throughout the heart during sinus rhythm and lead to a markedly more heterogeneous electrophysiological substrate.

(Received 14 May 2023; accepted after revision 11 December 2023; first published online 5 January 2024)
Corresponding author T. Gerach: Institute of Biomedical Engineering, Karlsruhe Institute of Technology (KIT), Kaiserstr. 12, 76131, Karlsruhe, Germany. Email: publications@ibt.kit.edu

Abstract figure legend Whole-heart electrophysiology is affected in several ways by mechano-electric feedback. Incorporating the mechanical deformation gradient into the monodomain equation alters tissue conductivity, ultimately resulting in a depolarization pattern that is more heterogeneous and leads to steeper repolarization gradients. Non-selective stretch-activated channels lead to a more heterogeneous diastolic transmembrane voltage and delayed repolarization or afterdepolarizations depending on the amount of stretch the tissue experiences. Accounting for calcium bound to troponin extends repolarization time, leading to an increase in calcium availability and larger stroke volumes. These mechanisms, when combined, may have implications for arrhythmogenesis relating to triggers and substrate.

Key points

- The electrophysiological and mechanical function of the heart are tightly interrelated by excitation–contraction coupling (ECC) in the forward direction and mechano-electric feedback (MEF) in the reverse direction.
- While ECC is considered in many state-of-the-art computational models of cardiac electromechanics, less is known about the effect of different MEF mechanisms.
- Accounting for calcium bound to troponin increases stroke volume and delays repolarization. Geometry-mediated MEF leads to more heterogeneous activation and repolarization with steeper gradients. Both effects combine in an additive way.
- Non-selective stretch-activated channels as an additional MEF mechanism lead to heterogeneous diastolic transmembrane voltage, higher developed tension and delayed repolarization or afterdepolarizations in highly stretched parts of the atria.
- The differential and combined effects of these three MEF mechanisms during sinus rhythm activation in a human four-chamber heart model may have implications for arrhythmogenesis, both in terms of substrate (repolarization gradients) and triggers (ectopy).

Introduction

The main function of the heart is that of a mechanical pump, supplying blood to all parts of the body. This pump, composed of billions of individual cells, is orchestrated electrically by electrophysiological excitation waves travelling through the myocardium. Once a cell is activated electrically and undergoes an action potential, calcium enters the cytosol both from the extracellular space as well as from the sarcoplasmic reticulum and initiates mechanical activation, a process known as excitation–contraction coupling (ECC) (Bers, 2002). In the reverse direction, mechano-electric feedback (MEF) describes the acute effects of the heart's mechanical status on its electrophysiology (Quinn & Kohl, 2021). The mechanisms by which MEF affects electrophysiology include effects on intracellular calcium handling, on conduction properties as well as activation or modulation of ion channels (Peyronnet et al., 2016). MEF has been shown to be involved in arrhythmogenesis in the atria and the ventricles, as reviewed by Quinn and Kohl (2021). The heart as an electromechanical system can adapt to different physiological demands in a remarkable range. In humans, for example, the blood volume pumped per

© 2024 The Authors. *The Journal of Physiology* published by John Wiley & Sons Ltd on behalf of The Physiological Society.

14697793, 0, Downloaded from https://physoc.onlinelibrary.wiley.com/doi/10.1113/JP285022 by Karlsruher Institut F., Wiley Online Library on [24/01/2024]. See the Terms and Conditions (https://onlinelibrary.wiley.com/terms-and-conditions) on Wiley Online Library for rules of use; OA articles are governed by the applicable Creative Commons License

minute can increase from around 5 l at rest to up to 35 l during very intense exercise. The electromechanical autoregulatory loop comprising ECC and MEF is an essential contributor to this adaptation capacity.

In recent decades, computational modelling and simulation have evolved to become a frequently used research tool in cardiac electrophysiology with first clinical applications (Trayanova et al., 2020). However, the temporally dynamic and spatially varying effect of mechanical function on electrophysiology is mostly neglected. So far, *in silico* studies have considered only selected MEF mechanisms without a systematic comparison (Augustin et al., 2016; Fedele et al., 2023; Moss et al., 2021; Zile & Trayanova, 2018) or have been limited to single-cell simulations (Balakina-Vikulova et al., 2020; Bartolucci et al., 2022; Healy & McCulloch, 2005; Hu & Sachs, 1997; Kohl & Sachs, 2001; Sachs, 1994; Timmermann et al., 2017), tissue slabs (Costabal et al., 2017; Margara et al., 2020) or (bi-)ventricular geometries (Petras et al., 2023; Salvador et al., 2022).

However, many aspects of the mechanical environment that cardiac tissue senses can only be reproduced in a whole-heart setting; for example, the spatially heterogeneous stretch in the atria during ventricular systole when the valve plane is being pulled towards the apex. In this study, we thus use our established four-chamber model of cardiac electromechanics (Gerach et al., 2021) to systematically assess the influence of three MEF mechanisms and their combinations on cardiac electrophysiology during physiological excitation (sinus rhythm): the reduction of free intracellular calcium due to binding to troponin C, the effects of deformation on tissue conductivity, and the integration of stretch-activated ion channels. Since the goal is to reproduce the entire mechano-electric regulatory loop with the model, changes in the electrical signal will also affect the mechanical response. Therefore, we also investigate how the integration of these MEF mechanisms affects the development of tension.

Materials and methods

We first introduce the anatomical model and the baseline electromechanical model used in this study. Building on this modelling framework, the three MEF mechanisms are detailed before describing the concrete *in silico* experiments.

Heart geometry

We used a previously developed whole-heart geometry (Gerach, 2022) based on magnetic resonance imaging (MRI) data of a 32-year-old healthy volunteer provided by Heidelberg University Hospital. The dataset was acquired using a 1.5T MR tomography system (Philips Medical Systems) and consists of a static whole-heart image at diastasis as well as time-resolved MRI in two-, three- and four-chamber long-axis views and 12 time-resolved short-axis slices with 10 mm spacing. As shown in Fig. 1, the heart was segmented, labelled, and partitioned into left ventricle (LV), right ventricle (RV), left atrium (LA), right atrium (RA), tricuspid valve (TV), mitral valve (MV), pulmonary valve (PV), aortic valve (AV), pulmonary veins, superior vena cava and inferior vena cava (combined as VEN), aorta and pulmonary artery (combined as ART), orifices (OR) of the atrial cavities, and the pericardium. The pericardium was further divided in an apical (AP) and basal (BP) section. The mechanical mesh was discretized with 128,976 linear tetrahedral elements using Gmsh (Geuzaine & Remacle, 2009). For electrophysiological simulations, a subset of the mechanical domain consisting only of the RA, LA, RV and LV was used and resolved with 7,363,776 linear tetrahedral elements. Additional subregions were annotated to account for transmural heterogeneity in the ventricles (endo, mid, epi) and fast conducting bundles in the atria (including crista terminalis, Bachmann's bundle and pectinate muscles). Myofibre orientation $\mathbf{Q} = \{\mathbf{f}_0, \mathbf{s}_0, \mathbf{n}_0\}$ was included using rule-based methods in the atria (Wachter et al., 2015) and the ventricles (Bayer et al., 2012; Schuler, 2021). Fibre angles were modelled as 66° on the endocardial and −41° on the epicardial surface based on diffusion tensor MRI data by Lombaert et al. (2012).

Computational model

The mathematical description and numerical solution of the electromechanically coupled heart model is based on our previously published and validated work (Gerach, 2022; Gerach et al., 2021). Therefore, we only summarize the most important parts here and focus on changes from the previous work in more detail.

Active and passive mechanics

The deformation of the heart during contraction and relaxation can be modelled by

$$\begin{cases} \rho \dfrac{\partial^2 \mathbf{d}}{\partial t^2} - \nabla \cdot \mathbf{FS} = \mathbf{0} & \text{in} \quad \Omega^0 \times (0, T], \\ \mathbf{FSN} = \mathbf{f}_\mathrm{C} & \text{on} \quad \Gamma^0_\mathrm{C} \times (0, T], \\ \mathbf{FSN} = -p_i(t) J \mathbf{F}^{-\top} \mathbf{N} & \text{on} \quad \Gamma^0_i \times (0, T], \\ \mathbf{d} = \mathbf{0} & \text{on} \quad \Gamma^0_\mathrm{D} \times (0, T], \end{cases} \tag{1}$$

with the density ρ, the displacement $\mathbf{d}$, the deformation gradient $\mathbf{F}$, its determinant $J = \det(\mathbf{F})$, the surface normal direction $\mathbf{N}$, and the second Piola–Kirchhoff stress $\mathbf{S}$. The

© 2024 The Authors. *The Journal of Physiology* published by John Wiley & Sons Ltd on behalf of The Physiological Society.

14697793, 0, Downloaded from https://physoc.onlinelibrary.wiley.com/doi/10.1113/JP285022 by Karlsruher Institut F., Wiley Online Library on [24/01/2024]. See the Terms and Conditions (https://onlinelibrary.wiley.com/terms-and-conditions) on Wiley Online Library for rules of use; OA articles are governed by the applicable Creative Commons License

second Piola–Kirchhoff stress combined the passive and active mechanical properties of myocardial tissue in an additive way:

$$\mathbf{S}\left(\mathbf{d}, T_{\mathrm{a}}\left(\left[\mathrm{Ca}^{2+}\right]_{\mathrm{i}}, \lambda, \dot{\lambda}\right)\right) = \begin{cases} \dfrac{\partial W(\mathbf{F})}{\partial \mathbf{F}} + T_{\mathrm{a}}\left(\left[\mathrm{Ca}^{2+}\right]_{\mathrm{i}}, \lambda, \dot{\lambda}\right) \dfrac{\mathbf{f}_0 \otimes \mathbf{f}_0}{\sqrt{\mathbf{F}\mathbf{f}_0 \cdot \mathbf{F}\mathbf{f}_0}} & \text{in } \Omega^0_{\mathrm{myo}}, \\ \dfrac{\partial W(\mathbf{F})}{\partial \mathbf{F}} & \text{in } \left\{\Omega^0 \setminus \Omega^0_{\mathrm{myo}}\right\}. \end{cases} \quad (2)$$

The passive behaviour of the myocardium $\Omega^0_{\mathrm{myo}} = \Omega^0_{\mathrm{LA}} \cup \Omega^0_{\mathrm{RA}} \cup \Omega^0_{\mathrm{LV}} \cup \Omega^0_{\mathrm{RV}}$ was defined by the orthotropic constitutive law of Usyk et al. (2000) with an additional volumetric term to enforce quasi-incompressibility:

$$\begin{aligned} W(\mathbf{F}) &= \frac{B}{2}(\ln(J))^2 + \frac{C}{2}\left(\exp(Q) - 1\right), \\ Q &= b_{\mathrm{ff}}E^2_{\mathrm{ff}} + b_{\mathrm{ss}}E^2_{\mathrm{ss}} + b_{\mathrm{nn}}E^2_{\mathrm{nn}} + b_{\mathrm{fs}}\left(E^2_{\mathrm{fs}} + E^2_{\mathrm{sf}}\right) \\ &\quad + b_{\mathrm{fn}}\left(E^2_{\mathrm{fn}} + E^2_{\mathrm{nf}}\right) + b_{\mathrm{ns}}\left(E^2_{\mathrm{ns}} + E^2_{\mathrm{sn}}\right), \end{aligned} \quad (3)$$

where $E_{\mathrm{kl}} = \mathbf{E}\mathbf{k}_0 \cdot \mathbf{l}_0$ for $k, l \in \{f, s, n\}$ (fibre, sheet, normal directions) are the entries of the Green–Lagrange strain tensor $\mathbf{E} = \frac{1}{2}(\mathbf{F}^{\mathrm{T}}\mathbf{F} - \mathbf{I})$. Tissue outside of the myocardium was defined by the hyperelastic energy potential

$$W(\mathbf{F}) = \frac{\mu}{2}\left(J^{-2/3}\mathbf{F} : \mathbf{F} - 3\right) + \frac{\kappa}{2}(J-1)^2, \quad (4)$$

of a neo-Hookean material with the shear modulus μ and the bulk modulus κ. The active tension $T_{\mathrm{a}}([\mathrm{Ca}^{2+}]_{\mathrm{i}}, \lambda, \dot{\lambda})$ produced by the contractile units of the sarcomere acted only in fibre direction $\mathbf{f}_0$ and was computed using the force model by Land et al. (2017); Land and Niederer (2018). It depends on the intracellular concentration of calcium $[\mathrm{Ca}^{2+}]_{\mathrm{i}}$, fibre stretch $\lambda = \sqrt{\mathbf{F}\mathbf{f}_0 \cdot \mathbf{F}\mathbf{f}_0}$, and fibre stretch rate $\dot{\lambda} = \frac{\mathrm{d}\lambda}{dt}$.

The movement of the heart is naturally constrained by the pericardial sac and other nearby organs. To model the effect of these constraints at the contact surface $\Gamma^0_{\mathrm{C}} = \Gamma^0_{\mathrm{M}} \cup \Gamma^0_{\mathrm{S}}$, we assumed a frictionless and permanent contact between the epicardium Γ^0_{M} and the surrounding tissues Γ^0_{S} represented by the domain Ω^0_{p}. The contact forces f_{C} can be interpreted as a linear spring between Γ^0_{M} and Γ^0_{S} with spring stiffness $K_{\perp}$ and act on the current surface normal of both surfaces but with opposite sign. For more details, we refer the reader to the original publication by Fritz et al. (2014). On the endocardial surface Γ^0_i, we applied normal stress boundary conditions to model the pressure p_i exerted by the blood on the chambers $i \in \{\mathrm{LA}, \mathrm{RA}, \mathrm{LV}, \mathrm{RV}\}$. The pressure p was calculated using a lumped parameter model of the circulatory system including heart valve dynamics as described previously (Gerach, 2022) with the parameters listed in Table B4. Finally, we imposed Dirichlet boundary conditions on the distal ends of the truncated pulmonary veins and venae cavae Γ^0_{D}, since we assumed little to no movement of the heart outside of the pericardium. All mechanical model parameters are given in Tables B2 and B3.

Electrophysiology

The spatio-temporal propagation of the transmembrane voltage V_{m} in the deformed heart is modelled by the monodomain equation:

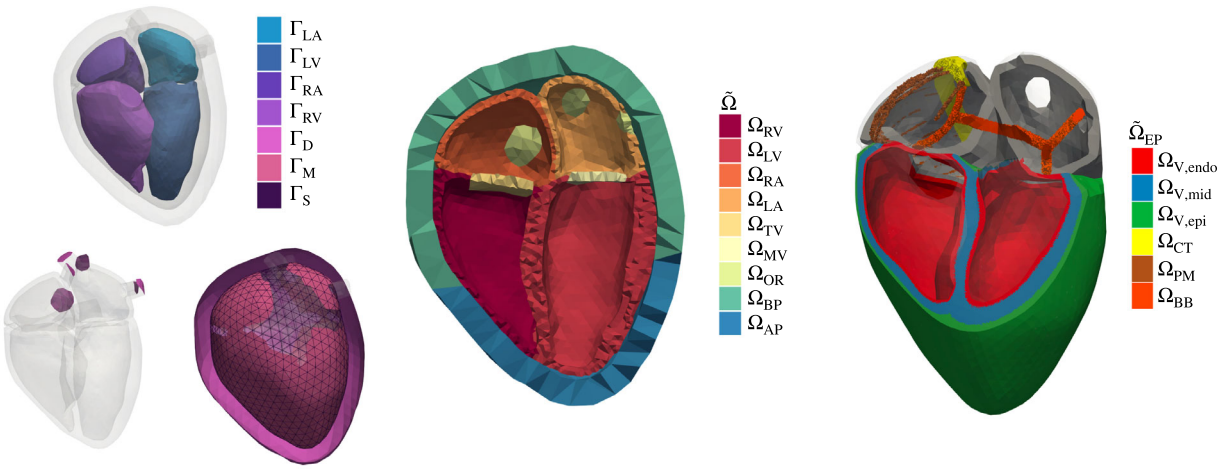

Figure 1. Heart model used for the electromechanical simulations
The left panel shows the surfaces Γ of the different anatomical structures. In the middle panel, the heart was clipped in the long-axis four-chamber view to reveal the labelled materials of the diastolic configuration of the volumetric mesh $\tilde{\Omega}$ used to compute deformation. In the electrophysiology mesh $\tilde{\Omega}_{\mathrm{EP}}$ (right panel), the myocardium was additionally labelled to account for transmural heterogeneity in the ventricles and fast-conducting bundles in the atria.

© 2024 The Authors. *The Journal of Physiology* published by John Wiley & Sons Ltd on behalf of The Physiological Society.

14697793, 0, Downloaded from https://physoc.onlinelibrary.wiley.com/doi/10.1113/JP285022 by Karlsruher Institut F., Wiley Online Library on [24/01/2024]. See the Terms and Conditions (https://onlinelibrary.wiley.com/terms-and-conditions) on Wiley Online Library for rules of use; OA articles are governed by the applicable Creative Commons License

$$\begin{cases} J\beta\left[C_{\mathrm{m}}\dfrac{\partial V_{\mathrm{m}}}{\partial t}+\hat{I}_{\mathrm{ion}}\left(V_{\mathrm{m}},\mathbf{u}_1,\mathbf{u}_2,\lambda\right)+I_{\mathrm{ext}}\left(t\right)\right]=\nabla\cdot\left(J\mathbf{F}^{-1}\mathbf{D}_{\mathrm{F}}\mathbf{F}^{-\mathrm{T}}\nabla V_{\mathrm{m}}\right) & \text{in } \Omega^0_{\mathrm{myo}},\\ \dfrac{\partial \mathbf{u}_1}{\partial t}-\mathbf{U}_1\ \left(V_{\mathrm{m}},\mathbf{u}_1,\lambda\right)=0 & \text{in } \left\{\Omega^0_{\mathrm{RA}}\cup\Omega^0_{\mathrm{LA}}\right\},\\ \dfrac{\partial \mathbf{u}_2}{\partial t}-\mathbf{U}_2\ \left(V_{\mathrm{m}},\mathbf{u}_2,\lambda\right)=0 & \text{in } \left\{\Omega^0_{\mathrm{RV}}\cup\Omega^0_{\mathrm{LV}}\right\},\\ \left(J\mathbf{F}^{-1}\mathbf{D}_{\mathrm{F}}\mathbf{F}^{-\mathrm{T}}\nabla V_{\mathrm{m}}\right)\cdot\mathbf{N}=0 & \text{on } \partial\Omega^0_{\mathrm{myo}}, \end{cases} \tag{5}$$

where β is the membrane surface-to-volume ratio, C_{m} is the specific membrane capacitance, and $\mathbf{D}_{\mathrm{F}}$ is the diffusion tensor in the deformed configuration. The anisotropy of cardiac tissue due to its preferential myocyte orientation ('fibre structure') is represented in the diffusion tensor

$$\mathbf{D}_{\mathrm{F}}=\sigma_f\frac{\mathbf{Ff}_0\otimes\mathbf{Ff}_0}{\|\mathbf{Ff}_0\|^2}+\sigma_s\frac{\mathbf{Fs}_0\otimes\mathbf{Fs}_0}{\|\mathbf{Fs}_0\|^2}+\sigma_n\frac{\mathbf{Fn}_0\otimes\mathbf{Fn}_0}{\|\mathbf{Fn}_0\|^2}, \tag{6}$$

by means of the tissue conductivities σ_f, σ_s, and σ_n in the fibre, sheet and normal directions, respectively. The ionic current $\hat{I}_{\mathrm{ion}}(V_{\mathrm{m}},\mathbf{u}_1,\mathbf{u}_2,\lambda)$ on the cellular level is defined by the vector valued functions $\mathbf{U}_1(V_{\mathrm{m}},\mathbf{u}_1,\lambda)$ (atria) and $\mathbf{U}_2(V_{\mathrm{m}},\mathbf{u}_2,\lambda)$ (ventricles) and the respective gating variables and ionic concentrations $\mathbf{u}_1$ and $\mathbf{u}_2$. In this work, we used the model by Courtemanche et al. (1998) for the atria. For the ventricles, we used the model by O'Hara et al. (2011) and modify the h- and j-gate as proposed by Passini et al. (2016) and Dutta et al. (2017). Since no dedicated model of pacemaker cells was included in the model, an external current $I_{\mathrm{ext}}(t)$ at the junction of the right atrial appendage and the superior vena cava was applied to mimic the sinoatrial node as well as five sites of earliest activation in the ventricles based on observations by Durrer et al. (1970) and simulation results obtained by Cardone-Noott et al. (2016) and Gillette et al. (2021). All parameters of the electrophysiological model are given in Table B1.

Mechano-electric feedback

MEF was included in our model on different scales. First, we implemented a MEF loop for the intracellular calcium concentration $[\mathrm{Ca}^{2+}]_{\mathrm{i}}$ into the ionic model equation $\mathbf{U}_1(V_{\mathrm{m}},\mathbf{u}_1,\lambda)$ and $\mathbf{U}_2(V_{\mathrm{m}},\mathbf{u}_2,\lambda)$ (Gerach et al., 2021; Levrero-Florencio et al., 2020; Margara et al., 2020). This feedback loop considers the binding of calcium ions to troponin C units

$$\frac{\partial \mathrm{CaTRPN}}{\partial t}=k_{\mathrm{TRPN}}\left[\left(\frac{\left[\mathrm{Ca}^{2+}\right]_{\mathrm{i}}}{\left[\mathrm{Ca}^{2+}\right]_{\mathrm{T50}}}\right)^{n_{\mathrm{TRPN}}}(1-\mathrm{CaTRPN})-\mathrm{CaTRPN}\right], \tag{7}$$

with the binding rate k_{TRPN}, the cooperativity of the binding rate n_{TRPN}, and the half activation point of calcium $[\mathrm{Ca}^{2+}]_{\mathrm{T50}}$ as described by Land et al. (2017). Since the calcium sensitivity of troponin C depends on the stretch state of the cell, we let $[\mathrm{Ca}^{2+}]_{\mathrm{T50}}$ be dependent on tissue stretch:

$$\left[\mathrm{Ca}^{2+}\right]_{\mathrm{T50}}=\left[\mathrm{Ca}^{2+}\right]_{\mathrm{T50}}(\lambda)=\left[\mathrm{Ca}^{2+}\right]^{\mathrm{ref}}_{\mathrm{T50}}+\beta_1\left(\min\left(\lambda,1.2\right)-1\right), \tag{8}$$

which effectively shifts the half activation point of calcium around a reference value $[\mathrm{Ca}^{2+}]^{\mathrm{ref}}_{\mathrm{T50}}$ based on the stretch λ and the sensitivity to stretch β_1. As a result of this MEF mechanism, the calcium bound to troponin during tension development is not available in the cytosol, thus lowering the intracellular concentration of calcium.

Second, we considered the effects of the deformation gradient $\mathbf{F}$ on the tissue level. Since $\mathbf{F}$ is dependent on the displacement $\mathbf{d}$ computed by the mechanics model eqn (1), the diffusion term $\nabla\cdot(J\mathbf{F}^{-1}\mathbf{D}_{\mathrm{F}}\mathbf{F}^{-\mathrm{T}}\nabla V_{\mathrm{m}})$ in eqn (5) accounts for the variations in the electrical properties due to the deformation of the tissue and the rotation of the fibres. As a matter of fact, if no deformation is present, i.e. $\mathbf{F}=\mathbf{I}$ and $J=1$, the monodomain eqn (5) returns to its standard form and MEF in the formulation of the diffusion tensor eqn (6) is neglected.

Finally, we considered the presence of non-specific stretch activated ion channels $I_{\mathrm{sac}}(V_{\mathrm{m}},\lambda)$ in the ionic current of the cellular models

$$\hat{I}_{\mathrm{ion}}\ \left(V_{\mathrm{m}},\mathbf{u}_1,\mathbf{u}_2,\lambda\right)=\begin{cases} I_{\mathrm{ion}}\left(V_{\mathrm{m}},\mathbf{u}_1\right)+I_{\mathrm{sac}}\left(V_{\mathrm{m}},\lambda\right)\ \text{in}\ \left\{\Omega^0_{\mathrm{RA}}\cup\Omega^0_{\mathrm{LA}}\right\},\\ I_{\mathrm{ion}}\left(V_{\mathrm{m}},\mathbf{u}_2\right)+I_{\mathrm{sac}}\left(V_{\mathrm{m}},\lambda\right)\ \text{in}\ \left\{\Omega^0_{\mathrm{RV}}\cup\Omega^0_{\mathrm{LV}}\right\}. \end{cases} \tag{9}$$

We used a simple representation of a stretch-activated channel first introduced by Sachs (1994) that successfully reproduced experimental observations in single-cell experiments:

$$I_{\mathrm{sac}}\ \left(V_{\mathrm{m}},\lambda\right)=\frac{G_{\mathrm{sac}}\left(V_{\mathrm{m}}-E_{\mathrm{sac}}\right)}{1+K\exp\left(-\alpha\left(\lambda-1\right)\right)}, \tag{10}$$

with the stretch-activated conductance $G_{\mathrm{sac}}=\gamma\varrho/C_{\mathrm{m}}$ as a product of the single channel conductance γ

© 2024 The Authors. The Journal of Physiology published by John Wiley & Sons Ltd on behalf of The Physiological Society.

14697793, 0, Downloaded from https://physoc.onlinelibrary.wiley.com/doi/10.1113/JP285022 by Karlsruher Institut F., Wiley Online Library on [24/01/2024]. See the Terms and Conditions (https://onlinelibrary.wiley.com/terms-and-conditions) on Wiley Online Library for rules of use; OA articles are governed by the applicable Creative Commons License

and channel density ϱ, the reversal potential E_{sac}, the equilibrium constant K, and the stretch sensitivity α. I_{sac} did not affect ion concentrations. Finding physiological parameters for I_{sac} in 3D tissue simulations is not straightforward as reports in the literature suggest a large variation in both their properties and their effect on action potential duration and morphology (Healy & McCulloch, 2005). The reversal potential E_{sac} has been measured in a wide range between -75 mV and 10 mV and measured conductance ranges from 10 pS to 200 pS (Hu & Sachs, 1997). The most commonly used parameters are $\gamma = 25$ pS, $\varrho = 0.3\ \mu\text{m}^{-2}$, $E_{\text{sac}} = -20$ mV, $K = 100$, and $\alpha = 3$ (Kohl & Sachs, 2001; Tavi et al., 1998; Zabel et al., 1996). However, with this parameterization, a stretch-activated current is present regardless of stretch, since the effective channel conductance is never zero. To avoid this, we increased the stretch sensitivity parameter to $\alpha = 20$, which effectively closes the channel at stretches <1. At higher stretches, this change in isolation would increase the current by a factor of 10 to 30 across the normal range of the transmembrane voltage. Therefore, we reduced the channel density ($\varrho = 0.015\ \mu\text{m}^{-2}$, 5% of the original value (Tavi et al., 1998)) and increased the equilibrium constant ($K = 150$). The parameters were mainly chosen such that I_{sac} does not trigger action potentials for $\lambda \leq 1.2$. This is supported by the sensitivity study presented in Appendix A. The effective channel conductance and current–voltage relationship of the stretch-activated channel used in this study is shown in Fig. 2.

Reference configuration and initial displacement

MRI data are typically acquired during the early diastolic state of the heart cycle when movement and chamber pressure are minimal. Because this diastolic pressure is non-zero, the mesh reconstructed from the MRI data corresponds to a pre-stressed configuration in diastole $\tilde{\Omega}$ (Fig. 1). However, residual stress in the tissue cannot be measured with standard imaging techniques. Therefore, a pressure-free reference configuration Ω^0 as the best estimate of the stress-free configuration of the heart has to be inferred to accurately model biomechanical function. We used the method proposed by Marx et al. (2022) to simultaneously identify passive tissue parameters and recover the stress-free reference configuration Ω^0 such that the end-diastolic pressure–volume relationship of the LV matches the data by Klotz et al. (2006). Since we did not have any invasive pressure measurements available for the heart used in this study, we assumed diastolic pressure to be $\tilde{p}_{\text{RV}} = 3.75$ mmHg, $\tilde{p}_{\text{RA}} = 4.5$ mmHg, $\tilde{p}_{\text{LV}} = 7.5$ mmHg, and $\tilde{p}_{\text{LA}} = 8.25$ mmHg. The initial displacement $\mathbf{d}_0$ was calculated by applying the diastolic pressure values to the stress-free reference configuration Ω^0. It immediately becomes clear that in the diastolic configuration, the displacement $\mathbf{d}$ is non-zero and thus $\mathbf{F} \neq \mathbf{I}$. Therefore, the electrical properties of the tissue change even without active contraction of the heart muscle.

Numerical simulations

The goal of this study is to isolate the effects of the different MEF mechanisms on activation and repolarization patterns as well as on tension development. Therefore, we performed a total of five simulations. In all of them, we solved the electromechanically coupled system given by eqns (1) and (5) in a segregated and staggered scheme (Gerach, 2022; Gerach et al., 2021) with different extents of MEF:

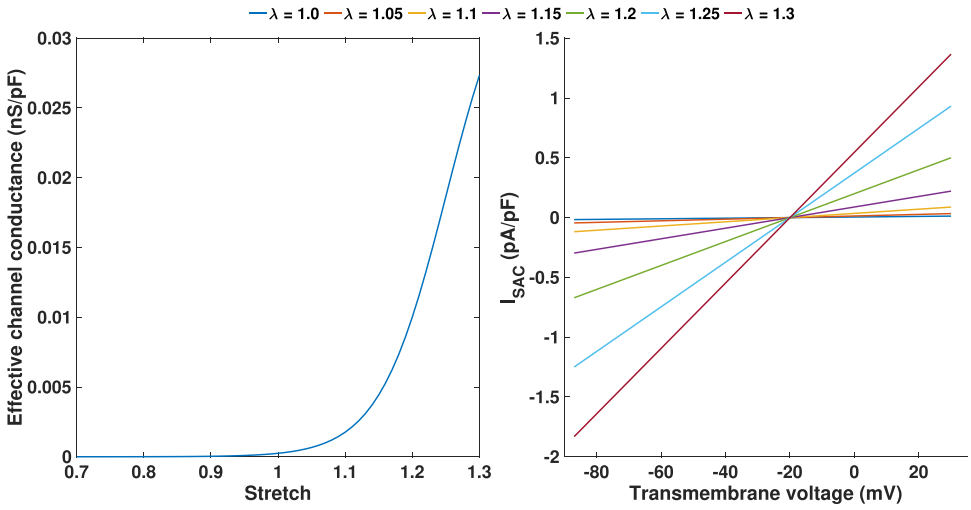

Figure 2. Stretch dependent behaviour of I_{sac}
Left: effective channel conductance with respect to stretch. Right: current–voltage relationship for different static stretches.

© 2024 The Authors. *The Journal of Physiology* published by John Wiley & Sons Ltd on behalf of The Physiological Society.

14697793, 0, Downloaded from https://physoc.onlinelibrary.wiley.com/doi/10.1113/JP285022 by Karlsruher Institut F., Wiley Online Library on [24/01/2024]. See the Terms and Conditions (https://onlinelibrary.wiley.com/terms-and-conditions) on Wiley Online Library for rules of use; OA articles are governed by the applicable Creative Commons License

(i) We ran the baseline simulation without any MEF. This is the standard case in the majority of cardiac electrophysiology and electromechanics studies and only involves ECC, i.e. the activation of tension development mediated by an increase of cytosolic calcium. Furthermore, this means eqn (5) is solved on the diastolic configuration $\Omega^0_{\text{myo}} = \tilde{\Omega}_{\text{myo}}$ with $\mathbf{F} = \mathbf{I}$ and $\lambda = 1$.

(ii) The cellular feedback of calcium binding to troponin C units described in eqns (7) and (8) was included in the simulation. Again, eqn (5) was solved on the diastolic configuration $\Omega^0_{\text{myo}} = \tilde{\Omega}_{\text{myo}}$ with $\mathbf{F} = \mathbf{I}$. However, λ is variable in this setup and was interpolated using the shape functions of the elements in the mechanics mesh before every electrophysiological compute step. This required setting up a linear mapping operator between the two meshes once before the simulation started.

(iii) We included the deformation gradient $\mathbf{F}$ in the diffusion term of the monodomain eqn (5) and the diffusion tensor (eqn 6).

(iv) We combined scenarios (ii) and (iii).

(v) Finally, we added the stretch-activated channel (eqn 10) to simulation scenario (iv).

In all cases, we simulated a total of three heartbeats which was sufficient to reach a limit cycle. Before that, the ionic models were stimulated for a total of 1000 cycles at 0.8 s basic cycle length in single-cell setups using $\lambda = 1$. To obtain a good initial approximation of the limit cycle of the circulatory system model, we performed purely mechanical simulations using local activation times from the solution of eqn (5) with $\mathbf{F} = \mathbf{I}$ on $\tilde{\Omega}_{\text{myo}}$. For these preliminary simulations, tension development was triggered at the time of activation by a static calcium transient extracted from the solution of eqn (5). Even though this simplified biophysical approach is more controllable than using a purely data-driven emulator (Regazzoni & Quarteroni, 2021), it is still a lot cheaper than letting every full electromechanical simulation converge to a limit cycle by itself from a less tailored initial state.

Results

As described above, five simulations with different levels of MEF were performed. The first simulation (i) considered no MEF and served as the baseline for the rest of the study. Figure 3 shows pressure–volume loops during the last heartbeat of each simulation. Additionally, the spatial fibre stretch distribution at four specific time steps is shown in Fig. 4 to demonstrate the large variations in strain during the different phases of the heartbeat. The baseline simulation reached an ejection fraction of about 50% in the LV, which corresponds to a stroke volume of around 100 ml. In diastole, the average fibre stretch in all four chambers was 1.07 ± 0.06. During atrial contraction, ventricular fibre stretch increased to around 1.15 with slightly higher values at the endocardium, while atrial fibre stretch reduced to around 0.8. This corresponds to a relative shortening of the fibres of up to 27%. The ventricles contracted to a much higher degree than the atria, since they started contraction in a pre-stretched

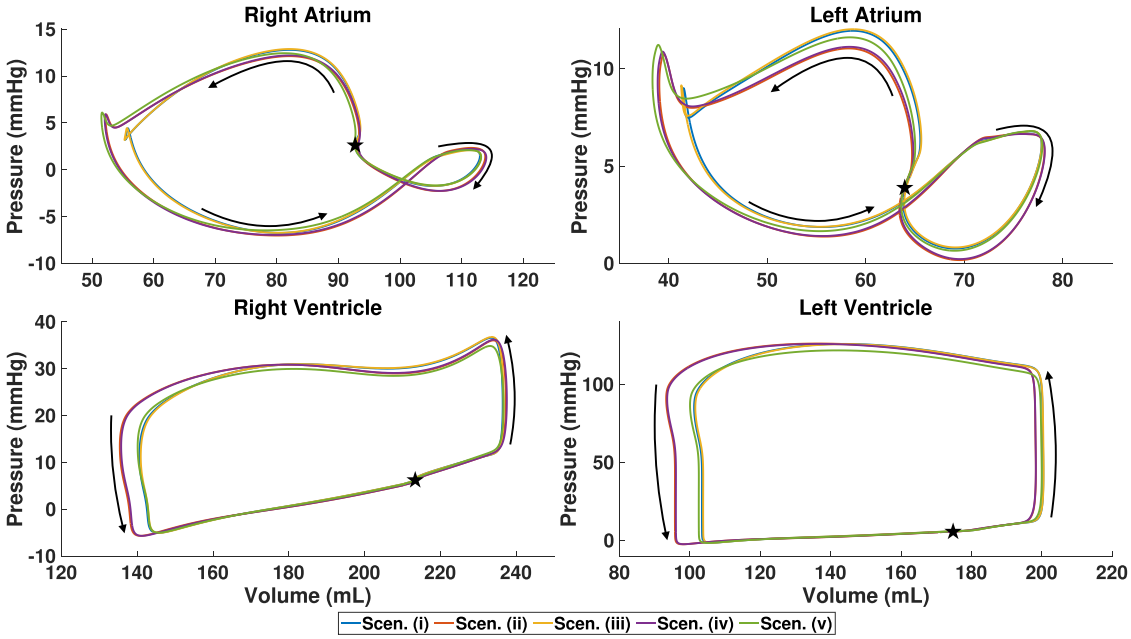

Figure 3. Pressure–volume loops for all simulations
The black star indicates the beginning of the heart cycle just before atrial contraction.

© 2024 The Authors. *The Journal of Physiology* published by John Wiley & Sons Ltd on behalf of The Physiological Society.

14697793, 0, Downloaded from https://physoc.onlinelibrary.wiley.com/doi/10.1113/JP285022 by Karlsruher Institut F., Wiley Online Library on [24/01/2024]. See the Terms and Conditions (https://onlinelibrary.wiley.com/terms-and-conditions) on Wiley Online Library for rules of use; OA articles are governed by the applicable Creative Commons License

position and finished at around the same stretch of 0.8. At the same time, the atria were stretched towards the atrio-ventricular valve plane. During this time frame of 200 ms to 300 ms, atrial fibres went from the fully shortened position to a full stretch at around 1.2.

Electrical activation of the atria and ventricles took around 100 ms each (Fig. 5). Repolarization to 90% of the peak V_m (APD90) was heterogeneous and lasted between 210 ms and 310 ms (Fig. 6). Areas with higher APD90 close to 300 ms include the crista terminalis and the subendocardial layer of the LV and RV. In particular, APD90 decreased gradually from subendocardial to the subepicardial layer in the ventricles.

For the second scenario (the simulation with troponin feedback (ii)), changes in the activation times of the myocardium were <1 ms. However, APD90 changed markedly. Especially in the atria, repolarization was prolonged by up to 50 ms. In the ventricles, the increase in APD90 was present as well but significantly less pronounced (<10 ms) and spatially more homogeneous. With this feedback mechanism, an additional increase in the intracellular calcium concentration during later times of the action potential was observed. The cross-over point at which the calcium concentration of the baseline simulation dropped below that of scenario (ii) was later in ventricular cells than atrial cells (Fig. 7). Both atrial and ventricular calcium transients became more action potential shaped due to the buffering in the contraction model including a faster rise of the intracellular calcium concentration (Fig. 7). Additionally, when

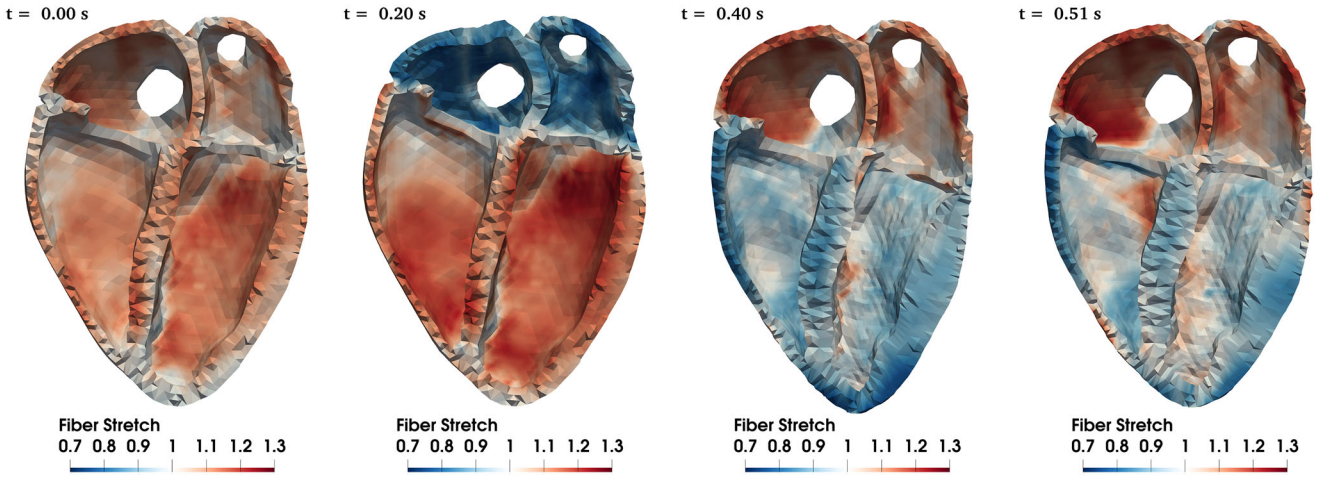

Figure 4. Deformation during sinus rhythm
Spatial distribution of fibre stretch and deformation of the heart in diastole, end of atrial contraction, end of ventricular contraction, and end of isovolumetric relaxation (baseline simulation, scenario (i)).

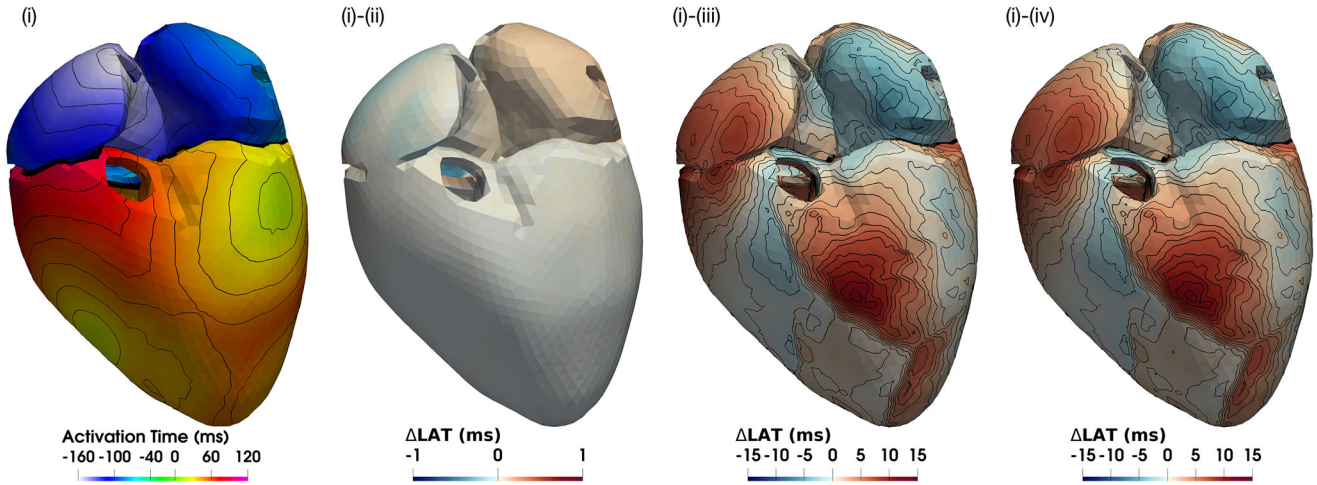

Figure 5. Activation times of scenarios (i) to (iv)
In scenarios (ii), (iii) and (iv), activation time differences with respect to the baseline simulation (i) are shown. Blue: activated later than baseline; red: activated earlier than baseline. Activation times were shifted by 160 ms (earliest ventricular activation). The colour scale was normalized per scenario.

© 2024 The Authors. *The Journal of Physiology* published by John Wiley & Sons Ltd on behalf of The Physiological Society.

14697793, 0, Downloaded from https://physoc.onlinelibrary.wiley.com/doi/10.1113/JP285022 by Karlsruher Institut F., Wiley Online Library on [24/01/2024]. See the Terms and Conditions (https://onlinelibrary.wiley.com/terms-and-conditions) on Wiley Online Library for rules of use; OA articles are governed by the applicable Creative Commons License

compared with the baseline simulation, the simulation with troponin feedback produces higher tension for a longer time, resulting in overall higher stroke volumes in all four chambers (Fig. 3).

In scenario (iii), only the deformation feedback on the diffusion term of the monodomain eqn (5) was considered. In terms of activation times, deviations from the baseline simulation of ±15 ms were observed. Compared with the baseline simulation, predominantly shorter APD90 values around the apex and the LA were observed, whereas APD90 was shorter in parts of the LV (Fig. 6). In general, changes were smaller than in scenario (ii), although much more heterogeneous.

The combination of scenarios (ii) and (iii) was simulated in scenario (iv). Activation times were very similar to scenario (iii) (Fig. 5), while APD90 mostly combined the effects of simulations (ii) and (iii) (Fig. 6). The heterogeneities introduced by the deformation feedback (iii) were present together with the shortened APD90 around the apex. The increased repolarization times in the atria matched those in scenario (ii).

Finally, a stretch-activated channel was introduced into the ionic models in both the atria and the ventricles. Compared with the other simulations, the resting membrane voltage increased by about 5 mV in the ventricles and 6 mV in the atria. Overall, resting membrane voltage became much more heterogeneous throughout the entire heart. This highly heterogeneous behaviour correlated directly with the distribution of fibre stretch as shown in Fig. 8. In particular, the base of the ventricles, the lateral free wall of the RA, and the posterior LA between the right and left pulmonary veins experienced large strain during diastole. These regions showed a depolarized resting membrane voltage by up to 13 mV. This particular change generally affected the atria more than the ventricles. With less than 3 ms difference, activation times did not change significantly compared with scenario (iv). Regarding repolarization, the general trend was a further increase of APD90. Some regions, predominantly in the atria, experienced large strain during ventricular contraction and exhibited delayed repolarization or afterdepolarizations (one location is shown in Fig. 7) before APD90 was reached leading to marked APD prolongation. The repolarization times of scenarios (i), (iv) and (v) are shown in Fig. 9. For scenario (iv), steeper repolarization gradients were observed on the anterior side of the LA, on both sides of the crista terminalis, and between the left inferior pulmonary vein and the MV. In scenario (v), this effect was even more pronounced with very steep gradients between the superior vena cava and the right atrial appendage, which coincides with the region of increased resting membrane voltage (Fig. 8).

Discussion

In this paper, we studied the effect of three different MEF mechanisms, individually and combined, in whole-heart simulations using our electromechanically coupled finite element framework. We analysed our findings with respect to activation and repolarization times as well as tension development.

The highly dynamic and spatially heterogeneous distribution of stretch during a sinus rhythm cycle in the human heart (Fig. 4) led to a number of heterogeneous effects mediated by the three MEF mechanisms considered in this study (reduction of free intracellular calcium due to binding to troponin C, effects of deformation on tissue conductivity, integration of stretch-activated ion channels).

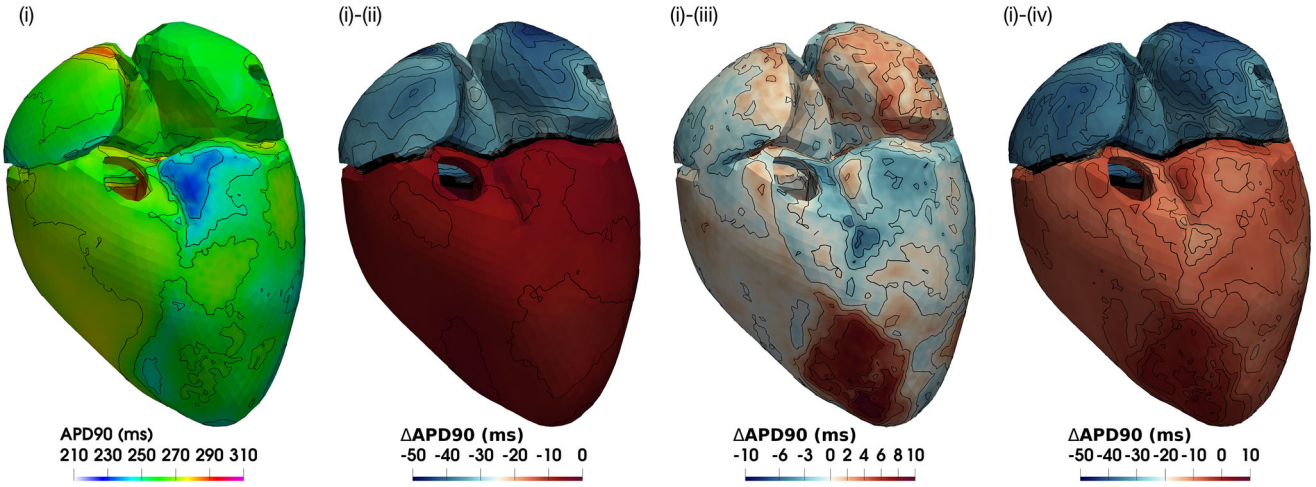

Figure 6. Action potential duration (APD90) of scenarios (i) to (iv)
In scenarios (ii), (iii) and (iv), APD90 differences with respect to the baseline simulation (i) are shown. Blue: longer APD90 than baseline; red: shorter APD90 than baseline.

© 2024 The Authors. *The Journal of Physiology* published by John Wiley & Sons Ltd on behalf of The Physiological Society.

14697793, 0, Downloaded from https://physoc.onlinelibrary.wiley.com/doi/10.1113/JP285022 by Karlsruher Institut F., Wiley Online Library on [24/01/2024]. See the Terms and Conditions (https://onlinelibrary.wiley.com/terms-and-conditions) on Wiley Online Library for rules of use; OA articles are governed by the applicable Creative Commons License

Calcium feedback increases stroke volume and delays repolarization but not activation

Including the effect of calcium binding to troponin C on electrophysiology leads to longer APD90 and later repolarization times (Fig. 6). Since in scenario (ii) the calcium transient amplitude is reduced and the plateau phase of the action potential is the consequence of calcium influx into the cell mostly balancing potassium efflux, these observations are expected and in line with previous reports. During repolarization, in contrast, the calcium concentration in the intracellular space is higher in scenario (ii) than in (i), which explains delayed repolarization. In our model, this effect was more pronounced in atrial cells than in ventricular cells. Augustin et al. (2016) coupled the Land tension model to the Grandi–Pasqualini–Bers model of myocyte electrophysiology, which led to longer APD90, lower calcium transient amplitude and slower calcium transient upstroke. Length-dependent calcium-binding affinity of troponin C led to higher calcium transients in the ventricles but reduced active stress. Atrial tension development was not considered in that study. Our simulations confirm these findings. Including the troponin bound calcium feedback in our model increased APD90 globally with a much larger increase in the atria (Fig. 6) and lowered the calcium transient amplitude (Fig. 7). Even though the peak calcium transient amplitude was lower, the calcium concentration remained higher for a longer time and resulted in a longer tension development. As a consequence, we observed larger stroke volumes in all four chambers (Fig. 3) while activation times were not affected by this feedback mechanism (Fig. 5).

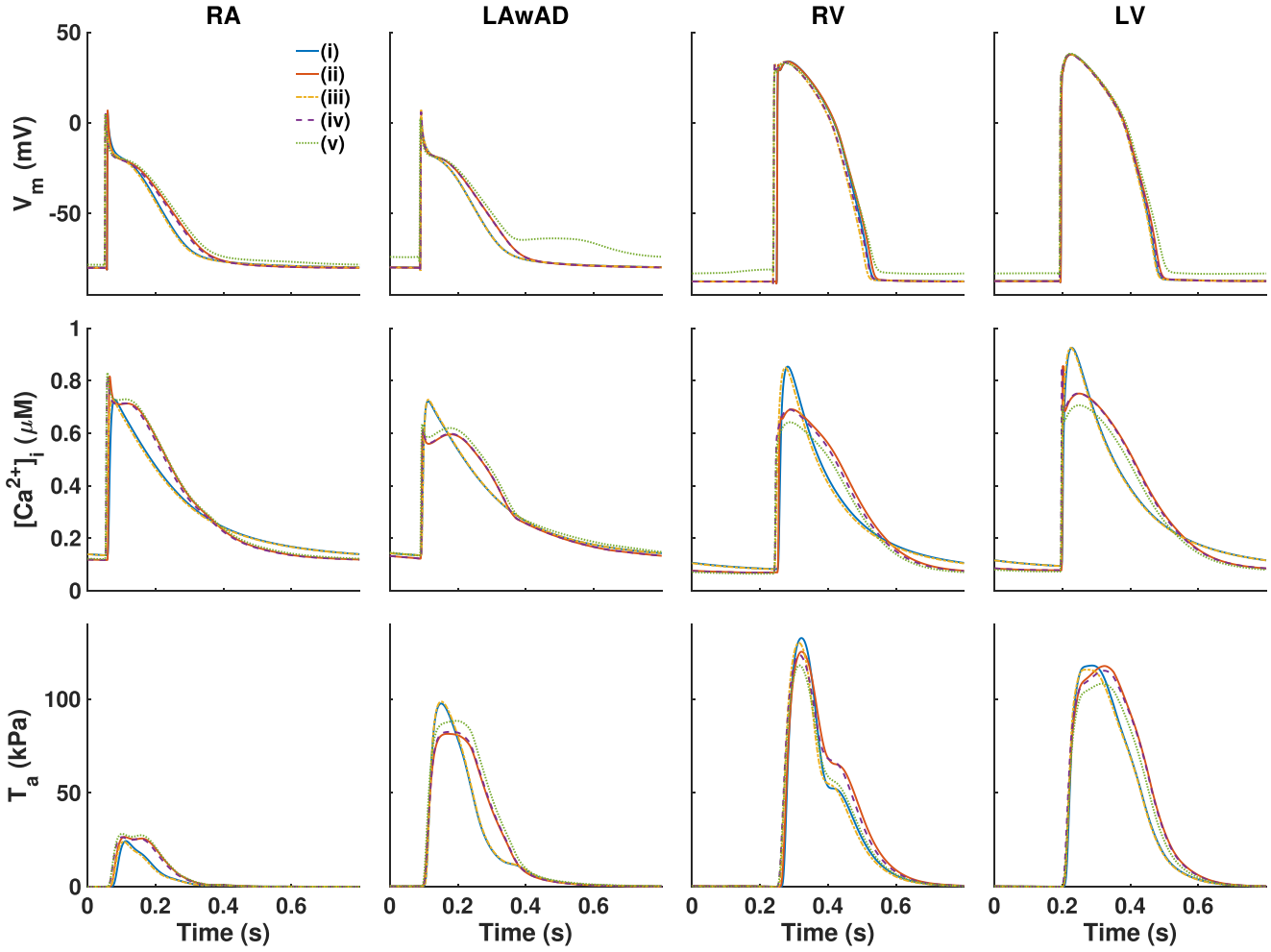

Figure 7. Transmembrane voltage V_m (top) and intracellular calcium concentration (middle) transients and active tension (bottom) for scenarios (i) to (v) at selected locations in the heart
RA: free wall right atrium; LAwAD: left atrium with the occurrence of an afterdepolarization/delayed repolarization in scenario (v); RV: free wall of the right ventricle; LV: middle of free wall left ventricle.

© 2024 The Authors. *The Journal of Physiology* published by John Wiley & Sons Ltd on behalf of The Physiological Society.

14697793, 0, Downloaded from https://physoc.onlinelibrary.wiley.com/doi/10.1113/JP285022 by Karlsruher Institut F., Wiley Online Library on [24/01/2024]. See the Terms and Conditions (https://onlinelibrary.wiley.com/terms-and-conditions) on Wiley Online Library for rules of use; OA articles are governed by the applicable Creative Commons License

Diffusion MEF leads to more heterogeneous activation and repolarization

The geometrical deformation in the monodomain diffusion tensor (scenario (iii)) affected the excitation propagation and led to altered activation times in the range of ±15 ms. Thus, some regions were activated earlier while others experienced delayed activation, which introduced a spatially more heterogeneous activation pattern. In particular, we observed earlier activation in the RA and in septal regions between the LV and RV (Fig. 5). Additionally, the geometrical feedback modulated APD90 (±10 ms) in a spatially heterogeneous manner. Shorter APD90 was observed around the ventricular apex and RV free wall as well as the LA, thus in regions with smaller diastolic stretch (Figs 4 and 6). Longer APD90 occurred mainly around the LV base and RA free wall, thus in regions with higher diastolic stretch.

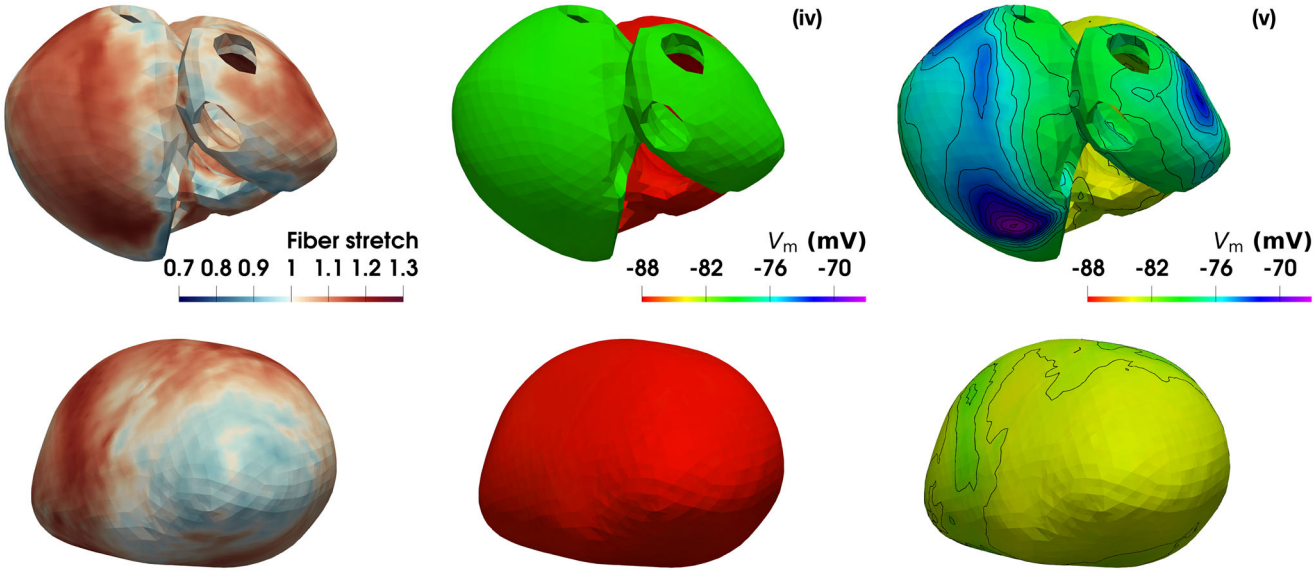

Figure 8. Fibre stretch and resting membrane voltage during diastole for scenarios (iv) and (v)
The top row shows the top-down perspective with view of both atria. The bottom row shows the bottom-up perspective with view of both ventricles.

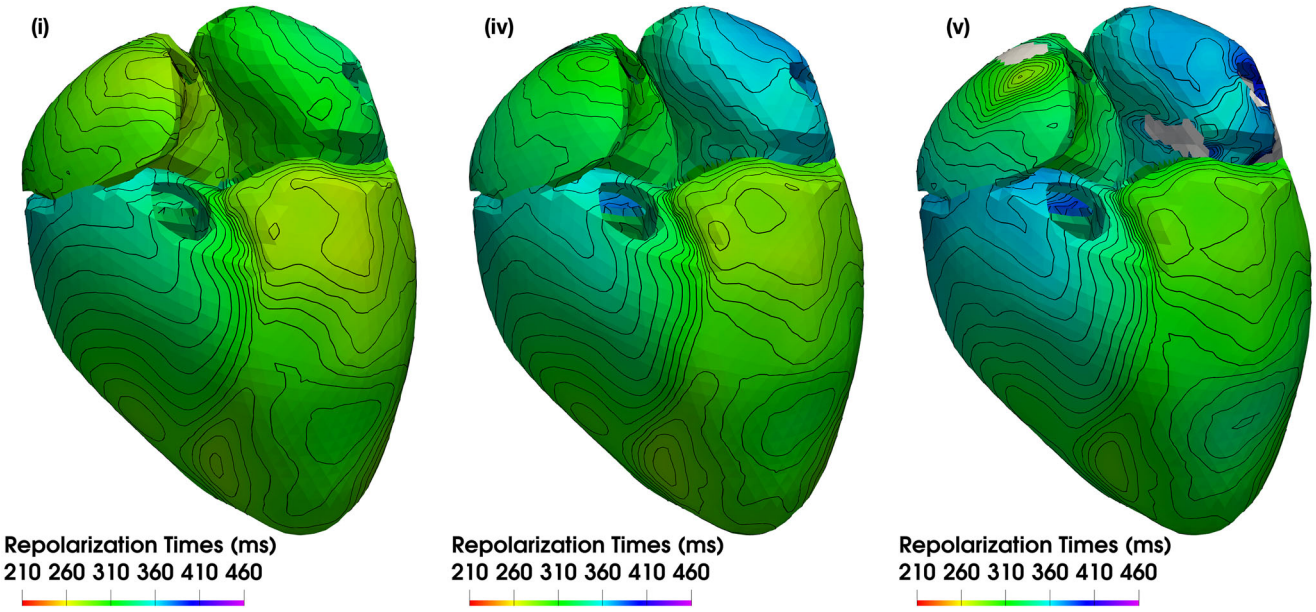

Figure 9. Repolarization times for scenarios (i), (iv) and (v)
Times in the ventricles were shifted by 160 ms (earliest ventricular activation) for better visualization. In scenario (v), the white patches are regions where afterdepolarizations occurred leading to repolarization times beyond 460 ms.

© 2024 The Authors. *The Journal of Physiology* published by John Wiley & Sons Ltd on behalf of The Physiological Society.

14697793, 0, Downloaded from https://physoc.onlinelibrary.wiley.com/doi/10.1113/JP285022 by Karlsruher Institut F., Wiley Online Library on [24/01/2024]. See the Terms and Conditions (https://onlinelibrary.wiley.com/terms-and-conditions) on Wiley Online Library for rules of use; OA articles are governed by the applicable Creative Commons License

The combined effects on activation and APD led to spatially heterogeneous modulation of repolarization time gradients (Fig. 9). These were steeper in the RV towards the septum, likely favouring the occurrence of unidirectional block and thus facilitating re-entry (Cluitmans et al., 2023). However, in most parts of the heart, the repolarization gradients were reduced by geometry-mediated MEF (repolarization isochrones more separated from one another in Fig. 9, particularly in the RA and the LV), which could be a relevant physiological mechanism for preventing the initiation of arrhythmia in the heart following a sinus rhythm activation.

It is important to understand that the impact of this feedback mechanism is highly dependent on the stress-free configuration and thus on the passive mechanical properties of the myocardium.

If the myocardium is stiffer, it will deform less when going from the stress-free reference configuration to the pre-stressed diastolic configuration as a baseline for the simulations. Compared with less stiff regions, diastolic tissue stretch will be smaller and therefore also the changes of the diffusion tensor due to the geometry-mediated MEF (eqn 6). Including the pericardial boundary conditions and potentially residual active tension when estimating the pressure-free reference configuration as demonstrated by Fedele et al. (2023) might alter the heterogeneous distribution of stretch as well. However, it is not clear yet how residual stress and the surrounding tissue alter stress and strain in the myocardium, since these can currently not be measured *in vivo* without the measurement affecting these quantities (Rodriguez et al., 1993).

The combined effects of calcium binding to troponin and geometrical deformation influencing the diffusion tensor (scenario (iv)) appear to affect MEF in an additive way.

I_{sac} leads to heterogeneous diastolic states and can favour ectopy

The inclusion of non-selective stretch-activated channels caused a spatially heterogeneous depolarization of resting membrane voltage (Fig. 8). The atria were more affected than the ventricles due to the reversal potential of −20 mV. The transmembrane voltage of the atrial model by Courtemanche et al. (1998) spends proportionally more time below this voltage than the ventricular action potential modelled according to O'Hara et al. (2011). As a result, the current I_{sac} is more depolarizing than repolarizing the atrial cells. In the ventricular model, the entire plateau phase is above the reversal potential and the resting membrane voltage is generally more negative than in the atria. Due to the direct correlation of the stretch-activated channel current with fibre stretch, this leads to a heterogeneous distribution of the resting membrane voltage, particularly in the atria with likely implications for excitability and conduction velocity due to effects on sodium channel availability as well as for ectopy.

The changes in the calcium concentration due to I_{sac} were rather small, but still affected the developed tension. In particular, ventricular calcium transients were reduced in amplitude upon inclusion of I_{sac} and thus less tension was developed while atrial calcium transients showed a small increase in amplitude leading to equal or more tension (Fig. 7).

Due to the depolarizing current at negative voltages below the reversal potential, I_{sac} delayed repolarization in the atria. Since repolarization in the atria is temporally linked with ventricular contraction, atrial tissue experiences large amounts of strain during systole (Varela et al., 2020). This increase in strain leads to larger I_{sac}. In our simulation, we observed several regions with afterdepolarizations or markedly delayed repolarization (Fig. 7) in the left and right atrium during ventricular contraction. Because entire groups of cells in a region with large strains experience this environment, this effect could be sufficient to overcome the source-sink mismatch (Xie et al., 2010) and initiate a stimulus that is captured by the surrounding myocardium. While we did not observe ectopic beats in our simulations, they are likely to occur in situations of enhanced I_{sac} conductance, enhanced strain, electrolyte imbalance, modulation of atrial APD, and in interplay with the spatially heterogeneous modulation of the resting membrane voltage (Fig. 8).

Ultimately, the stretch-activated channel led to markedly steeper repolarization gradients in some regions (Fig. 9). This behaviour was especially prominent in the LA and RA. As regions with higher repolarization gradients are linked to an increased chance of unidirectional block, I_{sac} might not only have a role in modulating arrythmia initiation via the likelihood of ectopic beats as discussed above but also have direct effects on the vulnerability of the substrate, thus on the full 'circle of re-entry' (Cluitmans et al., 2023).

Relating our findings to other previous work, Petras et al. (2023) showed that early depolarizations in the ventricles are possible with higher stretch sensitivity of I_{sac}. Additionally, they reported early repolarization areas in the subendocardial layer of both ventricles and the septum when including I_{sac} combined with a stretch and stretch rate dependent force generation model. In the absence of I_{sac} they did not observe any difference. Although early depolarization was not very pronounced in our study (<3 ms difference), the general trend points towards earlier depolarization when including the stretch-activated channel. However, we generally observed later repolarization times in the ventricles when including I_{sac}. Potentially this is caused by the use of different ionic models for the ventricles,

© 2024 The Authors. *The Journal of Physiology* published by John Wiley & Sons Ltd on behalf of The Physiological Society.

14697793, 0, Downloaded from https://physoc.onlinelibrary.wiley.com/doi/10.1113/JP285022 by Karlsruher Institut F., Wiley Online Library on [24/01/2024]. See the Terms and Conditions (https://onlinelibrary.wiley.com/terms-and-conditions) on Wiley Online Library for rules of use; OA articles are governed by the applicable Creative Commons License

different parameterizations of I_{sac}, different stretch in the biventricular canine *vs*. four-chamber human anatomical model or any combination of the former.

Salvador et al. (2022) reported an effect of geometry-mediated MEF and non-selective stretch-activated channels on ventricular tachycardia cycle length in a left ventricular model of electro-mechanics. In addition, the inclusion of stretch-activated channels led in some cases to transition from stable to unstable re-entrant dynamics or vice versa. Given the highly dynamic and nonlinear nature of re-entrant arrhythmias, it appears likely that the MEF-induced changes we observed during sinus rhythm could lead to similar qualitative changes during ventricular tachycardia. Considering that during re-entry, excitation can not only be driven by sodium currents but also by calcium (Nieuwenhuyse et al., 2017), the consequences of troponin bound to calcium might have additional significance beyond the pure APD prolongation (Fig. 6).

Limitations

Most of the limitations pertaining to the baseline model (Gerach et al., 2021) are also relevant for the investigation of MEF in this study. In addition, a number of specific limitations should be considered.

The change of the monodomain diffusion term in eqn (5) depending on the deformation gradient **F** is mathematically required for a correct solution. However, it is less clear how the baseline tissue conductivities **D** might be different during stretch. Considering that the number of cell-to-cell transitions per unit length will remain constant during acute stretch, the chosen approach might overestimate the effect. Using cell cultures on a polydimethylsiloxane substrate, Imboden et al. (2019) found a linear dependence of conduction velocity on strain (conduction velocity increases by 7% for a strain amplitude of 10%) in line with cable theory, assuming an axial to gap junction resistance ratio of 0.29:0.71. Globally, we saw a similar effect with activation time delays of around 10% (Fig. 5) in areas with diastolic stretch of around 10% (Fig. 4).

The parameters chosen for the stretch-activated channel formulation I_{sac} carry uncertainty. First, we limited this study to non-selective stretch-activated channels. Second, non-selective stretch-activated channels are well characterized in many aspects (Peyronnet et al., 2016) but their effective conductance in intact human tissue and its spatial heterogeneity (e.g. ventricles *vs*. atria) is unsatisfactorily constrained by experimental data. The afterdepolarizations observed in scenario (v) in highly stretched regions of the atria (Fig. 7) are a surprising finding and might on the one hand indicate an overestimation of the maximum channel conductance G_{sac} or other I_{sac}-related parameters. On the other hand, it could be a relevant contributor to ectopy in the atria involved in the arrhythmogenesis of, for example, atrial fibrillation (Quinn & Kohl, 2021). Based on these results, further experimental characterization of their role in intact human myocardium is warranted. The sensitivity study presented in Appendix A shows that the chosen parameters support the possibility of I_{sac} to trigger action potentials during high stretch ($\lambda \geq 1.24$) events as reported in the literature (Kohl & Sachs, 2001; Sachs, 1994). However, the atrial cell model is much more sensitive to the depolarizing stretch-activated current than the ventricular cell model. This may indicate a need for different parameterizations of atrial and ventricular cells. Given the mostly negative transmembrane voltage of the atrial cell model, a natural choice could be a more negative reversal potential such that I_{sac} has both depolarizing and repolarizing properties.

In this work, active stress was only applied in fibre direction (considering its change due to deformation). Some experimental results suggest that smaller shares of active stress also act directly in sheet and normal direction. Without MEF, cross-fibre active stress leads to more efficient pumping function; however, with a reduced twisting motion (Gerach et al., 2020). Future studies could evaluate whether these results are affected by geometry-mediated MEF.

Lastly, this study is limited to purely acute MEF effects during sinus rhythm. Additional mechanisms like long-term modulation of gene expression or structural remodelling as well as arrhythmias were not considered.

Conclusion

The *in silico* setting of this study allowed us to disentangle the differential and combined effects of different MEF mechanisms during sinus rhythm in a human whole-heart model. The spatially heterogeneous modulation of cardiac excitation conduction velocity and activation is mostly mediated by the effect of deformation on the diffusion term of the monodomain equation. In contrast, repolarization is also influenced by troponin-bound calcium and stretch-activated channels. While geometry-mediated MEF reduces repolarization gradients in many parts of the heart and can thus be considered an anti-arrhythmic physiological mechanism, troponin bound to calcium and, in particular, stretch-activated channels increased repolarization gradients. As the latter also led to delayed repolarization and afterdepolarizations in the atria, it seems that stretch-activated channels can exhibit pro-arrhythmic effects and favour re-entry both via increased probability for ectopy and for unidirectional block and are potential actionable targets clinically. Our

© 2024 The Authors. *The Journal of Physiology* published by John Wiley & Sons Ltd on behalf of The Physiological Society.

14697793, 0, Downloaded from https://physoc.onlinelibrary.wiley.com/doi/10.1113/JP285022 by Karlsruher Institut F., Wiley Online Library on [24/01/2024]. See the Terms and Conditions (https://onlinelibrary.wiley.com/terms-and-conditions) on Wiley Online Library for rules of use; OA articles are governed by the applicable Creative Commons License

results suggest that MEF mechanisms can be essential for studies which crucially depend on the heterogeneity of the electrophysiological substrate in terms of activation, conduction, or repolarization.

APPENDIX A: I_{sac} sensitivity study

To understand the impact of the different parameters given in the formulation of I_{sac} (eqn 10), we performed a sensitivity analysis on the single-cell level for both the atrial and ventricular cell model. The effective channel conductance depends on the parameters G_{sac}, K and α. Therefore, we first looked at the influence of these parameters on the effective channel conductance by varying them one at a time by ±25%, ±50% and ±75% of the baseline values given in Table B1. The results are shown in Fig. A1 and indicate that G_{sac} determines the maximum channel conductance at high values of λ, while K shifts the curve to lower (−25/50/75%) or higher (+25/50/75%) values of λ. α, on the other hand, changes how fast the effective channel conductance approaches the value of G_{sac}, which may not be possible for smaller values of α in the physiological range of λ. In particular, higher values of α will increase the channel conductance faster than lower values.

Since G_{sac} is the only parameter with a physiological meaning and single channel conductance and channel density are constrained well by other studies, we decided to keep the baseline value for this parameter. In the interval of $\lambda = [1.0, 1.3]$, the parameter α had the largest impact on the effective channel conductance. Therefore, we continued to test the influence of I_{sac} on the transmembrane voltage V_m by only varying α with the following protocol: Starting with the cell at rest ($\lambda = 1$), we subjected the cell to 8/12/16/20/24/28% stretch for 50 ms each with 450 ms of rest in between the stretch intervals. No external stimulus current was applied during this time. The results are shown in Fig. A2(*A*) for the ventricular model and Fig. A2(*B*) for the atrial model. Using baseline parameters, a stretch of 24% or higher resulted in a fully developed action potential. Less stretch resulted in an elevation of the transmembrane voltage for the duration of the applied stretch and returned to previous values immediately. This elevation of V_m during stretch was more pronounced in the atrial model (Fig. A2(*B*)) with approximately twice as much elevation as observed in the ventricular model (Fig. A2(*A*)). For all values of α, a stretch of 12% or less was not sufficient to induce an action potential. After increasing the value of α, the threshold of when an action potential was induced was lowered to 16% stretch (50% and 75% increase of α) or 20% stretch (25% increase of α). At smaller values of α compared with baseline, the produced current of I_{sac} was not sufficient to trigger an action potential in this setup.

Depending on the transmembrane voltage, the stretch-activated current can be either depolarizing or repolarizing (see Fig. 2). At which voltage the switch between depolarization and repolarization happens is determined by the reversal potential E_{sac}. Values reported in the literature for the reversal potential range from −75 mV to 10 mV (Hu & Sachs, 1997). Therefore, we used the same stretch protocol as before to evaluate how E_{sac} changes the cellular response to stretch using the baseline

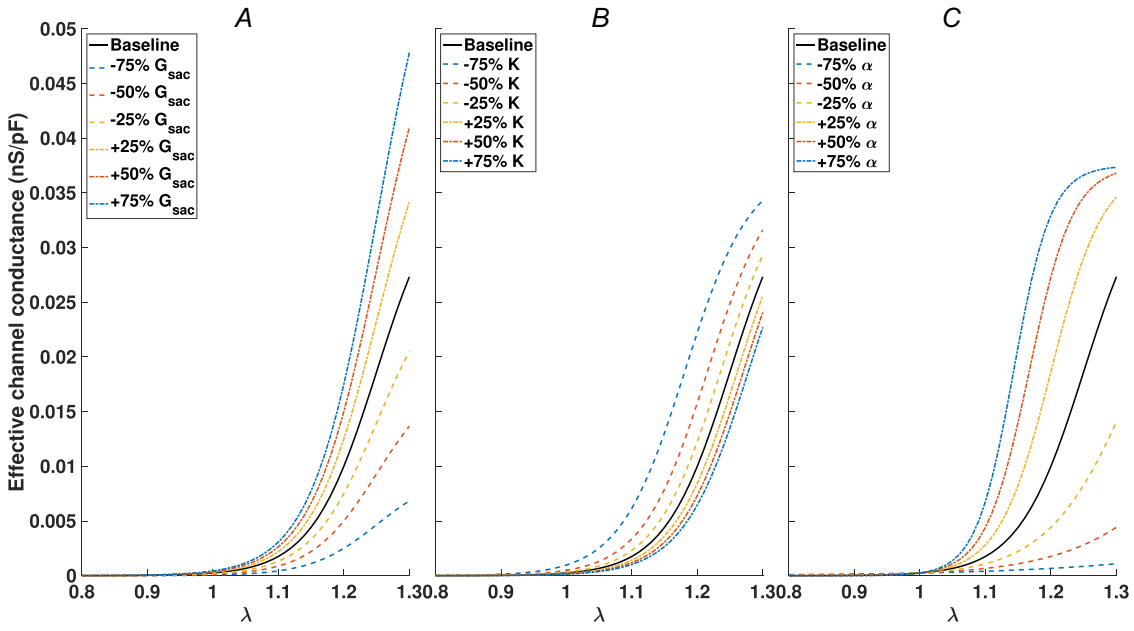

Figure A1.
The dependency of the effective channel conductance on the parameters (*A*) G_{sac}, (*B*) K, and (*C*) α.

© 2024 The Authors. *The Journal of Physiology* published by John Wiley & Sons Ltd on behalf of The Physiological Society.

14697793, 0, Downloaded from https://physoc.onlinelibrary.wiley.com/doi/10.1113/JP285022 by Karlsruher Institut F., Wiley Online Library on [24/01/2024]. See the Terms and Conditions (https://onlinelibrary.wiley.com/terms-and-conditions) on Wiley Online Library for rules of use; OA articles are governed by the applicable Creative Commons License

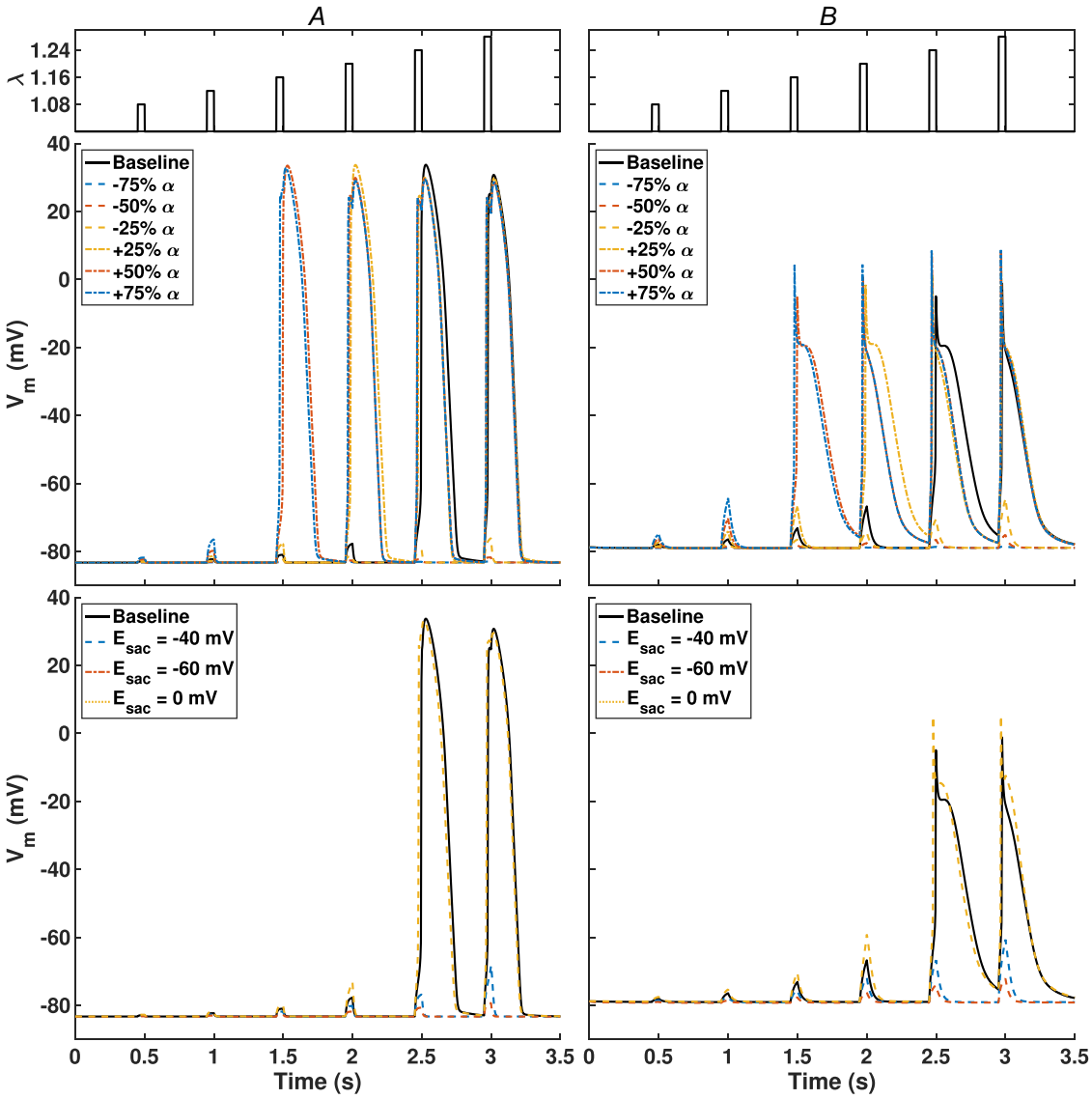

Figure A2.
The transmembrane voltage V_m as a result of continuously increasing stretch intervals (8/12/16/20/24/28% stretch) is shown for a ventricular cell (*A*) and an atrial cell (*B*)
The first row shows the stretch protocol. Additionally, the response of the cell model to the stretch protocol while varying α (second row) and E_{sac} (third row) is shown.

parameters in Table B1 and $E_{sac} = [0,-20,-40,-60]$ mV. The results are shown in the bottom row of Fig. A2. A reversal potential closer to 0 mV results in proportionally more depolarizing current, which is why $E_{sac} = 0$ mV and $E_{sac} = -20$ mV both trigger an action potential for stretches above 24%. If the reversal potential was more negative (-40 mV and -60 mV), thus closer to the resting membrane potential of the cell, the stretch-activated current was predominantly repolarizing and was no longer able to trigger action potentials.

APPENDIX B: Model parameters

Here, we provide the parameters of the numerical model in more detail. Parameters related to the electrophysiological model are given in Table B1. Anisotropic scaling of tissue conductivities and regional heterogeneities of ion channel conductances in the atria were taken from Loewe (2016). For the ionic models in the atria and ventricles, we used the original parameters reported in Courtemanche et al. (1998) and O'Hara et al.

© 2024 The Authors. *The Journal of Physiology* published by John Wiley & Sons Ltd on behalf of The Physiological Society.

14697793, 0, Downloaded from https://physoc.onlinelibrary.wiley.com/doi/10.1113/JP285022 by Karlsruher Institut F., Wiley Online Library on [24/01/2024]. See the Terms and Conditions (https://onlinelibrary.wiley.com/terms-and-conditions) on Wiley Online Library for rules of use; OA articles are governed by the applicable Creative Commons License

Table B1. Parameters of the electrophysiological model

Parameter	Value	Unit	Description
$(\sigma_f, \sigma_s, \sigma_n)$	(0.28, 0.182, 0.098)	S/m	Conductivities in ventricular myocardium
$(\sigma_f, \sigma_s, \sigma_n)$	(0.84, 0.546, 0.294)	S/m	Conductivities in ventricular subendocardial layer
$(\sigma_f, \sigma_s, \sigma_n)$	(0.68, 0.182, 0.182)	S/m	Conductivities in atrial myocardium
$(\sigma_f, \sigma_s, \sigma_n)$	(1.89, 0.212, 0.212)	S/m	Conductivities in Bachmann's bundle
$(\sigma_f, \sigma_s, \sigma_n)$	(1.28, 0.121, 0.121)	S/m	Conductivities in pectinate muscles
$(\sigma_f, \sigma_s, \sigma_n)$	(1.19, 0.182, 0.182)	S/m	Conductivities in crista terminalis
β	140,000	1/m	Membrane surface-to-volume ratio
C_m	0.01	F/m^2	Specific membrane capacitance
t_{RA}	0	ms	Initial time of stimulus current in RA
t_{LV}	(160, 160, 160)	ms	Initial time of stimulus current in LV
t_{RV}	(165, 172)	ms	Initial time of stimulus current in RV
BCL	0.8	s	Basic cycle length (= 1/heart rate)
Regional heterogeneities of ion channel conductances			
$(\hat{g}_{to}, \hat{g}_{Ca,L})$	(1.0, 1.67)	–	Scaling in crista terminalis
$(\hat{g}_{to}, \hat{g}_{Ca,L})$	(0.68, 1.06)	–	Scaling in atrial appendages
Stretch-activated channel			
α	20	–	Stretch sensitivity
γ	25	pS	Single channel conductance
ϱ	0.015	μm^{-2}	Channel density
K	150	–	Equilibrium constant
E_{sac}	-20	mV	Reversal potential

Table B2. Parameters of the active tension model

Parameter	Value	Unit	Description
k_{TRPN}	0.1	–	Binding rate
n_{TRPN}	2	–	Cooperativity of binding rate
β_0	0.7	–	Stretch dependence of tension
β_1	-1.2	–	Stretch dependence of calcium
$[Ca^{2+}]^{ref}_{T50}$	0.805	μM	Half activation point of calcium in ventricles
$[Ca^{2+}]^{ref}_{T50}$	0.86	μM	Half activation point of calcium in atria
ξ	2	–	Scaling factor for all crossbridge cycling rates in atria
T_{ref}	440	kPa	Reference tension in right ventricle
T_{ref}	400	kPa	Reference tension in left ventricle
T_{ref}	160	kPa	Reference tension in right atrium
T_{ref}	220	kPa	Reference tension in left atrium

(2011), respectively. Transmural heterogeneity in the ventricles was adopted from O'Hara et al. (2011) with changes proposed by Dutta et al. (2017). Parameters for the active tension model are based on Land et al. (2017); Land and Niederer (2018) and shown in Table B2. We modified the reference tension in each chamber of the heart to achieve physiological contractile behaviour and reduced the effect of stretch dependence to more reasonable levels. Passive mechanical properties are given in Table B3. Parameters C_{scale} and b_{scale} are the result of the simultaneous identification of myocardial tissue properties and the stress-free reference configuration based on the algorithm proposed by Marx et al. (2022) for the left ventricle. Due to a lack of data, we assumed that the overall material properties of myocardial tissue relate similarly in all chambers and applied the identified scaling parameters everywhere. Nevertheless, the base material stiffness of the right atrium and ventricle was increased by a factor of 1.66 and the left atrium by a factor of 2 (compared with the base value of C given in Table B3) to account for the higher amount of collagen present in these chambers (Oken & Boucek, 1957). The parameters of the lumped element circulatory system model are given in Table B4.

© 2024 The Authors. *The Journal of Physiology* published by John Wiley & Sons Ltd on behalf of The Physiological Society.

14697793, 0, Downloaded from https://physoc.onlinelibrary.wiley.com/doi/10.1113/JP285022 by Karlsruher Institut F., Wiley Online Library on [24/01/2024]. See the Terms and Conditions (https://onlinelibrary.wiley.com/terms-and-conditions) on Wiley Online Library for rules of use; OA articles are governed by the applicable Creative Commons License

Table B3. Parameters of the mechanical model

Parameter	Value	Unit	Description
B	650×10^3	Pa	Bulk modulus in the myocardium Ω_{myo}
C	880	Pa	Base material stiffness in the myocardium Ω_{myo}
b_{ff}	8	–	Fibre strain scaling in the myocardium Ω_{myo}
b_{ss}	6	–	Radial strain scaling in the myocardium Ω_{myo}
b_{nn}	3	–	Cross-fibre in-plain strain scaling in the myocardium Ω_{myo}
b_{fs}	12	–	Shear strain in f-s plane scaling in the myocardium Ω_{myo}
b_{fn}	3	–	Shear strain in f-n plane scaling in the myocardium Ω_{Myo}
b_{sn}	3	–	Shear strain in s-n plane scaling in the myocardium Ω_{myo}
C_{scale}^{LV}	0.042	–	Scaling for parameter C in domain Ω_{LV}
$C_{scale}^{RV,RA}$	0.07	–	Scaling for parameter C in domains $\{\Omega_{RV} \cup \Omega_{RA}\}$
C_{scale}^{LA}	0.084	–	Scaling for parameter C in domain Ω_{LA}
b_{scale}	3.55	–	Scaling for parameters b_{xx} in domain Ω_{myo}
$\mu^{MV,TV,AV,PV}$	1×10^6	Pa	Shear modulus in the valves
$\kappa^{MV,TV,AV,PV}$	650×10^3	Pa	Bulk modulus in the valves
μ^{OR}	7.45×10^3	Pa	Shear modulus in the domain Ω_{OR}
κ^{OR}	650×10^3	Pa	Bulk modulus in the domain Ω_{OR}
$\mu^{ART,VEN}$	15.18×10^3	Pa	Shear modulus in the domains $\{\Omega_{ART} \cup \Omega_{VEN}\}$
$\kappa^{ART,VEN}$	650×10^3	Pa	Bulk modulus in the domains $\{\Omega_{ART} \cup \Omega_{VEN}\}$
$\mu^{AP,BP}$	1×10^4	Pa	Shear modulus in the pericardial domains $\{\Omega_{AP} \cup \Omega_{BP}\}$
κ^{AP}	650×10^3	Pa	Bulk modulus in the apical pericardial domain Ω_{AP}
κ^{BP}	1×10^3	Pa	Bulk modulus in the basal pericardial domain Ω_{BP}
ρ	1082	kg^{-3}	Tissue density in the entire domain Ω
$K_\perp$	1×10^7	Pa	Contact penalty in normal direction on Γ_M

Table B4. Parameters of the circulatory system model

Parameter	Value	Unit	Description
Pulmonary and systemic circulation			
R_{SysArt}	0.05	$mmHg \cdot s \cdot ml^{-1}$	Systemic arterial resistance
C_{SysArt}	2.5	$ml \cdot mmHg^{-1}$	Systemic arterial compliance
$V_{SysArtUnstr}$	800.0	ml	Unstressed systemic arterial volume
R_{SysPer}	0.6	$mmHg \cdot s \cdot ml^{-1}$	Systemic peripheral resistance
R_{SysVen}	0.03	$mmHg \cdot s \cdot ml^{-1}$	Systemic venous resistance
C_{SysVen}	100.0	$ml \cdot mmHg^{-1}$	Systemic venous compliance
$V_{SysVenUnstr}$	2850.0	ml	Unstressed systemic venous resistance
R_{PulArt}	0.02	$mmHg \cdot s \cdot ml^{-1}$	Pulmonary arterial resistance
C_{PulArt}	10.0	$ml \cdot mmHg^{-1}$	Pulmonary arterial compliance
$V_{PulArtUnstr}$	150.0	ml	Unstressed pulmonary arterial volume
R_{PulPer}	0.07	$mmHg \cdot s \cdot ml^{-1}$	Pulmonary peripheral resistance
R_{PulVen}	0.03	$mmHg \cdot s \cdot ml^{-1}$	Pulmonary venous resistance
C_{PulVen}	15.0	$ml \cdot mmHg^{-1}$	Pulmonary venous compliance
$V_{PulVenUnstr}$	200.0	ml	Unstressed pulmonary venous volume
ρ_{Blood}	1060	kg/m^3	Blood density
Atrioventricular valves			
A_{Ref}	15.0	cm^2	Reference area
M_{max}	0.7	–	Maximum area ratio
M_{min}	0.001	–	Minimum area ratio

(*Continued*)

© 2024 The Authors. *The Journal of Physiology* published by John Wiley & Sons Ltd on behalf of The Physiological Society.

14697793, 0, Downloaded from https://physoc.onlinelibrary.wiley.com/doi/10.1113/JP285022 by Karlsruher Institut F., Wiley Online Library on [24/01/2024]. See the Terms and Conditions (https://onlinelibrary.wiley.com/terms-and-conditions) on Wiley Online Library for rules of use; OA articles are governed by the applicable Creative Commons License

Table B4. (Continued)

Parameter	Value	Unit	Description
K_o	20.0	$mmHg^{-1} \cdot s^{-1}$	Opening rate coefficient
K_c	6.0	$mmHg^{-1} \cdot s^{-1}$	Closing rate coefficient
Semilunar valves			
A_{Ref}	7.0	cm^2	Reference area
M_{max}	0.95	–	Maximum area ratio
M_{min}	0.001	–	Minimum area ratio
K_o	10.0	$mmHg^{-1} \cdot s^{-1}$	Opening rate coefficient
K_c	6.0	$mmHg^{-1} \cdot s^{-1}$	Closing rate coefficient

References

Augustin, C. M., Neic, A., Liebmann, M., Prassl, A. J., Niederer, S. A., Haase, G., & Plank, G. (2016). Anatomically accurate high resolution modeling of human whole heart electromechanics: A strongly scalable algebraic multigrid solver method for nonlinear deformation. *Journal of Computational Physics*, **305**, 622–646.

Balakina-Vikulova, N. A., Panfilov, A., Solovyova, O., & Katsnelson, L. B. (2020). Mechano-calcium and mechano-electric feedbacks in the human cardiomyocyte analyzed in a mathematical model. *The Journal of Physiological Sciences*, **70**(1), 1–23

Bartolucci, C., Forouzandehmehr, M., Severi, S., & Paci, M. (2022). A novel in silico electromechanical model of human ventricular cardiomyocyte. *Frontiers in Physiology*, **13**, 906146

Bayer, J. D., Blake, R. C., Plank, G., & Trayanova, N. A. (2012). A novel rule-based algorithm for assigning myocardial fiber orientation to computational heart models. *Annals of Biomedical Engineering*, **40**(10), 2243–2254.

Bers, D. M. (2002). Cardiac excitation–contraction coupling. *Nature*, **415**(6868), 198–205.

Cardone-Noott, L., Bueno-Orovio, A., Mincholé, A., Zemzemi, N., & Rodriguez, B. (2016). Human ventricular activation sequence and the simulation of the electrocardiographic QRS complex and its variability in healthy and intraventricular block conditions. *Europace*, **18**(S4), iv4–iv15.

Cluitmans, M. J. M., Bayer, J., Bear, L. R., Ter Bekke, R. M. A., Heijman, J., Coronel, R., & Volders, P. G. A. (2023). The circle of reentry: Characteristics of trigger-substrate interaction leading to sudden cardiac arrest. *Frontiers in Cardiovascular Medicine*, **10**, 1121517–1121517.

Costabal, F. S., Concha, F. A., Hurtado, D. E., & Kuhl, E. (2017). The importance of mechano-electrical feedback and inertia in cardiac electromechanics. *Computer Methods in Applied Mechanics and Engineering*, **320**, 352–368.

Courtemanche, M., Ramirez, R. J., & Nattel, S. (1998). Ionic mechanisms underlying human atrial action potential properties: Insights from a mathematical model. *American Journal of Physiology*, **275**(1 Pt 2), H301–H321.

Durrer, D., van Dam, R. T., Freud, G. E., Janse, M. J., Meijler, F. L., & Arzbaecher, R. C. (1970). Total excitation of the isolated human heart. *Circulation*, **41**(6), 899–912.

Dutta, S., Mincholé, A., Quinn, T. A., & Rodriguez, B. (2017). Electrophysiological properties of computational human ventricular cell action potential models under acute ischemic conditions. *Progress in Biophysics and Molecular Biology*, **129**, 40–52.

Fedele, M., Piersanti, R., Regazzoni, F., Salvador, M., Africa, P. C., Bucelli, M., Zingaro, A., Dede', L., & Quarteroni, A. (2023). A comprehensive and biophysically detailed computational model of the whole human heart electromechanics. *Computer Methods in Applied Mechanics and Engineering*, **410**, 115983.

Fritz, T., Wieners, C., Seemann, G., Steen, H., & Dössel, O. (2014). Simulation of the contraction of the ventricles in a human heart model including atria and pericardium: Finite element analysis of a frictionless contact problem. *Biomechanics and Modeling in Mechanobiology*, **13**(3), 627–641.

Gerach, T. (2022). Personalized electromechanical modeling of the human heart: Challenges and opportunities for the simulation of pathophysiological scenarios. PhD thesis, Karlsruher Institut fu¨r Technologie (KIT). https://doi.org/10.5445/IR/1000147806.

Gerach, T., Schuler, S., Fröhlich, J., Lindner, L., Kovacheva, E., Moss, R., Wülfers, E. M., Seemann, G., Wieners, C., & Loewe, A. (2021). Electro-mechanical whole-heart digital twins: A fully coupled multi-physics approach. *Mathematics*, **9**(11), 1247.

Gerach, T., Schuler, S., Kovacheva, E., Doessel, O., & Loewe, A. (2020). Consequences of using an orthotropic stress tensor for left ventricular systole. *Computing in Cardiology Conference (CinC)*. https://doi.org/10.22489/CinC.2020.246

Geuzaine, C., & Remacle, J. F. (2009). Gmsh: A 3-D finite element mesh generator with built-in pre-and post-processing facilities. *International Journal for Numerical Methods in Engineering*, **79**(11), 1309–1331

Gillette, K., Gsell, M. A. F., Bouyssier, J., Prassl, A. J., Neic, A., Vigmond, E. J., & Plank, G. (2021). Automated framework for the inclusion of a his–purkinje system in cardiac digital twins of ventricular electrophysiology. *Annals of Biomedical Engineering*, **49**(12), 3143–3153.

Healy, S. N., & McCulloch, A. D. (2005). An ionic model of stretch-activated and stretch-modulated currents in rabbit ventricular myocytes. *EP Europace*, **7**(s2), S128–S134.

© 2024 The Authors. *The Journal of Physiology* published by John Wiley & Sons Ltd on behalf of The Physiological Society.

14697793, 0, Downloaded from https://physoc.onlinelibrary.wiley.com/doi/10.1113/JP285022 by Karlsruher Institut F., Wiley Online Library on [24/01/2024]. See the Terms and Conditions (https://onlinelibrary.wiley.com/terms-and-conditions) on Wiley Online Library for rules of use; OA articles are governed by the applicable Creative Commons License

Hu, H., & Sachs, F. (1997). Stretch-activated ion channels in the heart. *Journal of Molecular and Cellular Cardiology*, **29**(6), 1511–1523.

Imboden, M., de Coulon, E., Poulin, A., Dellenbach, C., Rosset, S., Shea, H., & Rohr, S. (2019). High-speed mechano-active multielectrode array for investigating rapid stretch effects on cardiac tissue. *Nature Communications*, **10**(1), 834.

Klotz, S., Hay, I., Dickstein, M. L., Yi, G. H., Wang, J., Maurer, M. S., Kass, D. A., & Burkhoff, D. (2006). Single-beat estimation of end-diastolic pressure-volume relationship: A novel method with potential for noninvasive application. *American Journal of Physiology-Heart and Circulatory Physiology*, **291**(1), H403–H412.

Kohl, P., & Sachs, F. (2001). Mechanoelectric feedback in cardiac cells. *Philosophical Transactions of the Royal Society of London Series A: Mathematical, Physical and Engineering Sciences*, **359**(1783), 1173–1185.

Land, S., & Niederer, S. A. (2018). Influence of atrial contraction dynamics on cardiac function. *International Journal for Numerical Methods in Biomedical Engineering*, **34**(3), e2931.

Land, S., Park-Holohan, S. J., Smith, N. P., Dos Remedios, C. G., Kentish, J. C., & Niederer, S. A. (2017). A model of cardiac contraction based on novel measurements of tension development in human cardiomyocytes. *Journal of Molecular and Cellular Cardiology*, **106**, 68–83.

Levrero-Florencio, F., Margara, F., Zacur, E., Bueno-Orovio, A., Wang, Z. J., Santiago, A., Aguado-Sierra, J., Houzeaux, G., Grau, V., Kay, D., Vázquez, M., Ruiz-Baier, R., & Rodriguez, B. (2020). Sensitivity analysis of a strongly-coupled humanbased electromechanical cardiac model: Effect of mechanical parameters on physiologically relevant biomarkers. *Computer Methods in Applied Mechanics and Engineering*, **361**, 112762.

Loewe, A. (2016). *Modeling human atrial patho-electrophysiology from ion channels to ECG-substrates, pharmacology, vulnerability, and P-waves* (vol. **23**). KIT Scientific Publishing. https://doi.org/10.5445/KSP/1000054615

Lombaert, H., Peyrat, J. M., Croisille, P., Rapacchi, S., Fanton, L., Cheriet, F., Clarysse, P., Magnin, I., Delingette, H., & Ayache, N. (2012). Human atlas of the cardiac fiber architecture: Study on a healthy population. *IEEE Transactions on Medical Imaging*, **31**(7), 1436–1447.

Margara, F., Wang, Z. J., Levrero-Florencio, F., Santiago, A., Vázquez, M., Bueno-Orovio, A., & Rodriguez, B. (2020). In-silico human electro-mechanical ventricular modelling and simulation for drug-induced pro-arrhythmia and inotropic risk assessment. *Progress in Biophysics and Molecular Biology*, **159**, 58–74.

Marx, L., Niestrawska, J. A., Gsell, M. A. F., Caforio, F., Plank, G., & Augustin, C. M. (2022). Robust and efficient fixed-point algorithm for the inverse elastostatic problem to identify myocardial passive material parameters and the unloaded reference configuration. *Journal of Computational Physics*, **463**, 111266.

Moss, R., Wülfers, E. M., Schuler, S., Loewe, A., & Seemann, G. (2021). A fully-coupled electro-mechanical whole-heart computational model: Influence of cardiac contraction on the ECG. *Frontiers in Physiology*, **12**, 778872.

Nieuwenhuyse, E. V., Seemann, G., Panfilov, A. V., & Vandersickel, N. (2017). Effects of early afterdepolarizations on excitation patterns in an accurate model of the human ventricles. *PLoS ONE*, **12**(12), e0188867.

O'Hara, T., Virág, L., Varró, A., & Rudy, Y. (2011). Simulation of the undiseased human cardiac ventricular action potential: Model formulation and experimental validation. *PLoS Computational Biology*, **7**(5), e1002061.

Oken, D. E., & Boucek, R. J. (1957). Quantitation of collagen in human myocardium. *Circulation Research*, **5**(4), 357–361.

Passini, E., Mincholé, A., Coppini, R., Cerbai, E., Rodriguez, B., Severi, S., & Bueno-Orovio, A. (2016). Mechanisms of pro-arrhythmic abnormalities in ventricular repolarisation and anti-arrhythmic therapies in human hypertrophic cardiomyopathy. *Journal of Molecular and Cellular Cardiology*, **96**, 72–81.

Petras, A., Gsell, M. A. F., Augustin, C. M., Rodriguez-Padilla, J., Jung, A., Strocchi, M., Prinzen, F. W., Niederer, S. A., Plank, G., & Vigmond, E. J. (2023). Mechanoelectric effects in healthy cardiac function and under left bundle branch block pathology. *Computers in Biology and Medicine*, **156**, 106696.

Peyronnet, R., Nerbonne, J. M., & Kohl, P. (2016). Cardiac mechano-gated ion channels and arrhythmias. *Circulation Research*, **118**(2), 311–329.

Quinn, T. A., & Kohl, P. (2021). Cardiac mechano-electric coupling: Acute effects of mechanical stimulation on heart rate and rhythm. *Physiological Reviews*, **101**(1), 37–92.

Regazzoni, F., & Quarteroni, A. (2021). Accelerating the convergence to a limit cycle in 3D cardiac electromechanical simulations through a data-driven 0D emulator. *Computers in Biology and Medicine*, **135**, 104641.

Rodriguez, E. K., Omens, J. H., Waldman, L. K., & McCulloch, A. D. (1993). Effect of residual stress on transmural sarcomere length distributions in rat left ventricle. *American Journal of Physiology-Heart and Circulatory Physiology*, **264**(4), H1048–H1056.

Sachs, F. (1994). Modeling mechanical-electrical transduction in the heart. *Cell Mechanics and Cellular Engineering*, 308–328. https://doi.org/10.1007/978-1–4613–8425-018

Salvador, M., Regazzoni, F., Pagani, S., Dede', L., Trayanova, N., & Quarteroni, A. (2022). The role of mechano-electric feedbacks and hemodynamic coupling in scar-related ventricular tachycardia. *Computers in Biology and Medicine*, **142**, 105203.

Schuler, S. (2021). [SW] KIT-IBT/LDRB Fibers v1.0. Zenodo https://doi.org/10.5281/zenodo.4606575

Tavi, P., Han, C., & Weckström, M. (1998). Mechanisms of stretch-induced changes in [ca2+] i in rat atrial myocytes: Role of increased troponin c affinity and stretch-activated ion channels. *Circulation Research*, **83**(11), 1165–1177.

Timmermann, V., Dejgaard, L. A., Haugaa, K. H., Edwards, A. G., Sundnes, J., McCulloch, A. D., & Wall, S. T. (2017). An integrative appraisal of mechano-electric feedback mechanisms in the heart. *Progress in Biophysics and Molecular Biology*, **130**(Pt B), 404–417

Trayanova, N. A., Doshi, A. N., & Prakosa, A. (2020). How personalized heart modeling can help treatment of lethal arrhythmias: A focus on ventricular tachycardia ablation strategies in post-infarction patients. *Wiley Interdisciplinary Reviews: Systems Biology and Medicine*, **12**(3), e1477.

© 2024 The Authors. *The Journal of Physiology* published by John Wiley & Sons Ltd on behalf of The Physiological Society.

14697793, 0, Downloaded from https://physoc.onlinelibrary.wiley.com/doi/10.1113/JP285022 by Karlsruher Institut F., Wiley Online Library on [24/01/2024]. See the Terms and Conditions (https://onlinelibrary.wiley.com/terms-and-conditions) on Wiley Online Library for rules of use; OA articles are governed by the applicable Creative Commons License

Usyk, T., Mazhari, R., & McCulloch, A. (2000). Effect of laminar orthotropic myofiber architecture on regional stress and strain in the canine left ventricle. *Journal of Elasticity*, **61**(1/3), 143–164.

Varela, M., Queiros, S., Anjari, M., Correia, T., King, A. P., Bharath, A. A., & Lee, J. (2020). Strain maps of the left atrium imaged with a novel high resolution CINE MRI protocol. *Annual International Conference of the IEEE Engineering in Medicine and Biology Society. IEEE Engineering in Medicine and Biology Society. Annual International Conference*, **2020**, 1178–1181.

Wachter, A., Loewe, A., Krueger, M. W., Dössel, O., & Seemann, G. (2015). Mesh structure-independent modeling of patient-specific atrial fiber orientation. *Current Directions in Biomedical Engineering*, **1**(1), 409–412.

Xie, Y., Sato, D., Garfinkel, A., Qu, Z., & Weiss, J. N. (2010). So little source, so much sink: Requirements for afterdepolarizations to propagate in tissue. *Biophysical Journal*, **99**(5), 1408–1415.

Zabel, M., Koller, B. S., Sachs, F., & Franz, M. R. (1996). Stretch-induced voltage changes in the isolated beating heart: Importance of the timing of stretch and implications for stretch-activated ion channels. *Cardiovascular Research*, **32**(1), 20–130.

Zile, M. A., & Trayanova, N. A. (2018). Increased thin filament activation enhances alternans in human chronic atrial fibrillation. *American Journal of Physiology-Heart and Circulatory Physiology*, **315**(5), H1453–H1462.

Additional information

Data availability statement

The original contributions presented in the study are included in the article, further inquiries can be directed to the corresponding author.

Competing interests

All authors declare that they have no conflict of interest.

Author contributions

T. G.: Conceptualization, Methodology, Software, Investigation, Analysis, Writing – Original Draft, Visualization. A. L.: Conceptualization, Analysis, Writing – Review & Editing, Supervision, Funding acquisition. All authors approved the final version of the manuscript.

Funding

This research was funded by Deutsche Forschungsgemeinschaft (DFG, German Research Foundation) – Project-ID 258734477 – SFB 1173 and LO 2093/6-1 (SPP 2311).

Acknowledgements

The authors acknowledge support from the state of Baden-Württemberg through bwHPC. The authors would also like to thank Marie Houillon for her help with the software and infrastructure at the institute, and Jonathan Krauß for the lively discussions on mechanics.

Open access funding enabled and organized by Projekt DEAL.

Keywords

computer modelling and simulation, mechano-electric feedback, monodomain, repolarization gradient, stretch-activated channels

Supporting information

Additional supporting information can be found online in the Supporting Information section at the end of the HTML view of the article. Supporting information files available:

Peer Review History

© 2024 The Authors. *The Journal of Physiology* published by John Wiley & Sons Ltd on behalf of The Physiological Society.

14697793, 0, Downloaded from https://physoc.onlinelibrary.wiley.com/doi/10.1113/JP285022 by Karlsruher Institut F., Wiley Online Library on [24/01/2024]. See the Terms and Conditions (https://onlinelibrary.wiley.com/terms-and-conditions) on Wiley Online Library for rules of use; OA articles are governed by the applicable Creative Commons License